Selective retention of extracellular polymeric substances induced by adsorption to and coprecipitation with ferrihydrite

Ming Zhang [a], Caroline L. Peacock [b], Peng Cai [a,*], Ke-Qing Xiao [b], Chenchen Qu [a], Yichao Wu [a], Qiaoyun Huang [a]

[a] *State Key Laboratory of Agricultural Microbiology, College of Resources and Environment, Huazhong Agricultural University, Wuhan 430070, China*
[b] *School of Earth and Environment, University of Leeds, Leeds LS2 9JT, UK*

Abstract

Recent work shows that microbially-derived compounds constitute a significant fraction of the soil organic matter (OM) pool. These compounds include extracellular polymeric substances (EPS) whose mass can far exceed total microbial cell biomass. Sorption of EPS to soil minerals occurs via adsorption and coprecipitation and contributes to the preservation of OM in the soil environment. Little is known, however, about the sorption mechanisms of EPS and selective retention of different EPS constituents on iron (oxyhydr)oxides, especially during EPS adsorption versus coprecipitation with these reactive soil phases. This study examines how EPS interacts with the ubiquitous soil iron (oxyhydr)oxide ferrihydrite during EPS adsorption and coprecipitation and whether these different EPS-mineral association pathways affect EPS sorption and selective retention, and thus the mobility and fate of microbially-derived OM in the soil environment. We use several complimentary techniques to i) examine EPS-carbon, EPS-nitrogen and EPS-phosphorus sorption and fractionation, ii) visualize spatial relationships between EPS biomolecular classes and ferrihydrite using confocal laser scanning microscopy (CLSM), iii) determine EPS-C speciation and chemical fractionation with ferrihydrite using X-ray photoelectron spectroscopy (XPS) and near-edge X-ray absorption fine structure spectroscopy (NEXAFS), and iv) determine functional group interactions with ferrihydrite using Fourier transform infrared spectroscopy (FTIR) combined with two-dimensional correlation spectroscopy (2D-COS) analysis. Results show that the coprecipitation of EPS does not change the ferrihydrite mineralogy, as the main mineral phase for EPS association, but it substantially increases the particle size of EPS-ferrihydrite. A substantial difference in the EPS mass fraction associated with the ferrihydrite is observed between the adsorption and coprecipitation experiments at an initial molar C/Fe ratio >1. The EPS-N is relatively enriched during the adsorption process, while more EPS-C and near-complete EPS-P are fixed in the coprecipitation process. XPS results show that the surface of the ferrihydrite formed through EPS adsorption is preferentially enriched with protein-like components, whereas, the surface of the ferrihydrite formed through EPS coprecipitation is enriched with polysaccharide-like components, which is visually confirmed with CLSM images. NEXAFS results reveal that the carboxylic/amide C-containing components are selectively retained during adsorption, with the aliphatic and O-alkyl C-containing components relatively enriched during coprecipitation. 2D-FTIR-COS results indicate that during EPS adsorption on ferrihydrite the P=O functional groups are adsorbed faster than the amide and carboxylate functional groups, while during EPS coprecipitation with ferrihydrite the opposite trend is observed. The findings from this study indicate that the formation pathway of EPS-ferrihydrite associations substantially effects the sorption mechanisms and selective retention of EPS and may thus affect the mobility and fate of microbially-derived carbon (C), nitrogen (N) and phosphorus (P) in soils. These new insights on EPS behaviour at the mineral–water interface might be used to

---

* Corresponding author.
E-mail address: cp@mail.hzau.edu.cn (P. Cai).

evaluate how microbially-derived compounds like EPS are stabilized by iron (oxyhydr)oxides and how EPS-iron (oxyhydr) oxide couplings might affect the reactivity and cycling of OM in natural environments.

1. INTRODUCTION

Microorganisms are of great importance to the cycles of many elements such as carbon, nitrogen and phosphorus (Xu et al., 2013). In addition to their role in the degradation of organic matter (OM), particularly plant-derived compounds, microbial exudation products, biofilms and necromass all contribute to soil OM as microbially-derived compounds (Beveridge et al., 1997). In the past decade or so, there has been a greater recognition that microbial products may dominate inputs into soil OM pools, with microbially-derived compounds recently estimated to account for the primary constituents (50–80%) of soil OM (Simpson et al., 2007; Liang and Balser, 2011; Miltner et al., 2012; Kallenbach et al., 2016). Of particular interest are extracellular polymeric substances (EPS), which are produced continuously by microorganisms during their growth and metabolism (Flemming and Wingender, 2010; Flemming et al., 2016). The mass of these compounds can far exceed (up to 500%) total microbial cell biomass (Or et al., 2007; Chenu and Cosentino, 2011) and account for 80% of biofilm dry mass (Chenu, 1993). In general EPS are hydrated, heterogeneous mixtures of biopolymers composed predominantly of polysaccharides and proteins, with nucleic acids and lipids as minor constituents (Guibaud et al., 2008). These substances can control the biological and physicochemical properties of biofilms, and offer microorganisms protection against various environmental stresses (dehydration, pollution, predation, etc.) (Costa et al., 2018).

Once EPS are released into soil environments, the interaction between EPS and soil minerals can affect a broad variety of biogeochemical processes. These include the formation and growth of biofilms on soil substrates (Ma et al., 2017; Wu et al., 2019), the aggregation, transformation and stability of soil minerals (Lin et al., 2018; Huang et al., 2020), and how these EPS-mineral composites interact with essential elements and contaminants and control their fixation and ultimate mobility (Couasnon et al., 2019; Yan et al., 2019). In particular, the sorption of EPS by soil minerals constitutes an important process for the retention and stabilization of OM in soils, and in particular for the preservation of polysaccharides, proteins and lipids (Kleber et al., 2015). What is less clear however, is whether and how changes in the way EPS is taken up by soil minerals effects the sequestration of specific EPS constituents, and thus ultimately the reactivity and cycling of OM in soils.

The sorption of EPS by soil minerals can occur via both surface adsorption onto mineral particles and during the coprecipitation of minerals with EPS, and is a key process in the stabilization of EPS against microbial degradation in soils (Omoike and Chorover, 2006; Mikutta et al., 2011). The heterogeneous composition of EPS leads to a complex sorption behaviour. Adsorption of EPS onto soil mineral surfaces (goethite, montmorillonite and kaolinite) tends to follow a reverse adsorption pH edge, with decreasing adsorption with increasing pH (Lin et al., 2016). Adsorbed amount of EPS also decreases with decreasing ionic strength (Cao et al., 2011), indicating that at least some part of the EPS-mineral association occurs via outer-sphere electrostatic interactions (Omoike and Chorover, 2006). Adsorption of EPS onto goethite however, is dominated by inner-sphere ligand exchange reactions between surficial Fe-OH groups and P-containing EPS functional groups (Omoike and Chorover, 2006; Fang et al., 2012). Coprecipitation of EPS with soil minerals is less investigated but is a key phenomenon in a variety of soil processes, such as mineral formation and transformation induced by microorganisms (Chan et al., 2009; Jubb et al., 2018). It is also likely to play an important role in the sorption, retention and stabilization of OM by minerals. In particular, it is often observed in natural soils and sediments that carbon-mineral couplings have C/Fe molar ratios far in excess of those expected for adsorption, suggesting that coprecipitation of OM into mineral pore spaces and aggregates might be a dominant control on OM reactivity and cycling (Kaiser and Guggenberger, 2007; Wagai and Mayer, 2007; Lalonde et al., 2012). Indeed, coprecipitation of *Bacillus subtilis*-derived EPS with Al (hydr)oxides is shown to reduce mineralisation rates (Mikutta et al., 2011).

During the sorption of EPS by soil minerals, EPS extracted from liquid cultures often undergoes chemical fractionation of the EPS constituents (Poggenburg et al., 2018b). During adsorption to goethite, EPS extracted from *B. subtilis* is chemically and physically fractionated, with preferential adsorption of proteins, particularly those with high-molecular weight, and phosphorylated macromolecules (Omoike and Chorover, 2004; Omoike and Chorover, 2006). During adsorption to ferrihydrite and bentonite, preferential adsorption of P-rich and high-molecular weight EPS components is observed on ferrihydrite, compared to selective retention of N-rich and low-molecular weight EPS components on bentonite (Mikutta et al., 2012). During both adsorption and coprecipitation on Al hydroxide, there is preferential sorption of nucleic acids and polysaccharides, with an affinity for proteins less clearly observed (Mikutta et al., 2011).

Whilst the sorption and subsequent fractionation of EPS have been investigated with a variety of soil minerals, the sorption behaviour of EPS via its adsorption and coprecipitation with ferrihydrite remains comparatively

poorly known. This is problematic because ferrihydrite is ubiquitous in soils and possesses an extremely high sorption capacity as a result of its nanoparticulate nature, high surface area and reactivity, and is commonly found associated with OM (Cismasu et al., 2011; Basile-Doelsch et al., 2020). The sorption behaviour of EPS with ferrihydrite might be similar to the sorption of low molecular weight organic moieties and natural OM with ferrihydrite, short-range-ordered Fe (oxyhydr)oxides and bateriogenic Fe oxides, the latter of which are commonly found to consist of ferrihydrite adsorbed and coprecipitated with OM (Ferris, 2005; Fortin and Langley, 2005). During coprecipitation with ferrihydrite, the sorption of organic moieties chosen as model EPS compounds is higher for polymers with more carboxyl C (polygalacturonic acid > alginate > xanthan) (Mikutta et al., 2008). A range of organic moieties with differing complexity and natural OM isolated from a variety of terrestrial environments also sorb to ferrihydrite, short-range-ordered Fe (oxyhydr)oxides and bateriogenic Fe oxides via carboxyl functional groups (Gu et al., 1994; Gu et al., 1995; Kaiser and Guggenberger, 2000; Lv et al., 2016; Sowers et al., 2018; Sowers et al., 2019). Scanning transmission X-ray microscopy (STXM) analysis shows however, that during coprecipitation of natural OM with ferric iron, different functional groups are sorbed in spatially distinct regions, but that polysaccharide OM strongly spatially correlates with Fe (oxyhydr)oxides and binding strength is positively correlated to the presence of polysaccharide carboxyl C (Henneberry et al., 2012). During iron biomineralization, STXM analysis also shows that polysaccharide carboxyl groups bind with ferric iron to produce bacteriogenic iron oxides (Chan et al., 2009). These studies suggest therefore that EPS sorption to ferrihydrite will depend on the interaction of specific functional groups with the mineral particles, and that in particular, carboxyl groups might play an important role in EPS sequestration. It remains to be determined however, which functional groups are important for EPS adsorption and coprecipitation with ferrihydrite, and whether these different EPS-mineral association pathways effect EPS sorption and selective retention.

This study determines the sorption mechanisms and selective retention of EPS during its adsorption and coprecipitation with ferrihydrite. Our objectives are four fold and we achieve these using several complimentary techniques: i) To compare bulk EPS-C, EPS-N and EPS-P sorption and fractionation in EPS-ferrihydrite adsorption complexes and coprecipitates; ii) To visualize the spatial distribution of biomolecular compound classes in EPS-ferrihydrite adsorption complexes and coprecipitates using confocal laser scanning microscopy (CLSM); iii) To determine the organic C speciation, likely functional group interactions and thus the chemical fractionation of EPS components in EPS-ferrihydrite adsorption complexes and coprecipitates using X-ray photoelectron spectroscopy (XPS) and C 1s near edge X-ray absorption fine structure spectroscopy (NEXAFS); and iv) To further explore functional group interactions and determine the order in which different groups interact with the ferrihydrite particles in EPS-

ferrihydrite adsorption complexes and coprecipitates using Fourier transform infrared (FTIR) spectroscopy combined with two-dimensional correlation spectroscopy (2D-COS). Our investigation provides new information on the sorption and selective retention of EPS with ferrihydrite, with implications for EPS stability during microbial degradation and thus the mobility and fate of C, N and P in the soil environment.

2. MATERIALS AND METHODS

2.1. Extraction and characterization of extracellular polymeric substances

Extracellular polymeric substances (EPS) were extracted from *Bacillus subtilis* SBE1 (China Center for Type Culture Collection, CCTCC AB 2018210). The *Bacillus* genus is not only widely known to produce biofilms and EPS, and be the dominant soil aggregating bacteria (Costa et al., 2018), but EPS extracted from *Bacillus* is also commonly used as a representative EPS substance in biofilm and EPS research (Liu et al., 2013; Kovács, 2019). This specific strain has been isolated from soil and studied in our previous work where it can form biofilms in the presence of soil iron oxides (Ma et al., 2017). *B. subtilis* SBE1 were added to LB-Lennox Medium (5 g L^{-1} yeast extract, 10 g L^{-1} tryptone, 5 g L^{-1} NaCl) under aerobic conditions. The cells were incubated at 28 °C and 180 rpm in flasks placed on a horizontal shaker until the early stationary (24 h) growth phase (Omoike and Chorover, 2006). EPS was isolated from the suspension solution as described by Lin et al. (2016). Briefly, the bacterial cells were removed from the suspension by centrifugation (5000*g*, 15 min, 4 °C). The decanted supernatant was centrifuged again (12,000*g*, 15 min, 4 °C) to remove residual cells. EPS was precipitated from the collected supernatant by adding cold reagent-grade ethanol at a ratio of 1:3 (v/v supernatant/ethanol). After 48-h storage at 4 °C, the precipitate was separated from the mixture by centrifugation (12,000*g*, 15 min, 4 °C). To remove residual medium and impurities including ethanol, the EPS pellets obtained by centrifugation were dialyzed using cellulose membranes (Spectrum, 3500 MWCO). After 72-hour dialysis with three changes of Milli-Q water per day, the purified EPS solution was freeze-dried and stored at 4 °C until use (Omoike and Chorover, 2006).

Total organic C and N of the EPS were determined using a multi N/C 2100 analyzer (Analytik Jena, Jena, Germany). Total organic P of the EPS was determined via digestion with potassium peroxydisulfate (K$_2$S$_2$O$_8$) and measurement using the molybdenum blue spectrophotometric method (GB 11893–89). Polysaccharides were measured by the phenol–sulfuric acid method (DuBois et al., 1956). Proteins were assayed by bicinchoninic acid (BCA) protein assay kit (Biosharp, Anhui, China). Nucleic acid was determined using a NanoDrop 2000 Spectrophotometer (Thermo Scientific, Waltham, MA, USA). For each measurement three sub samples of the EPS were chosen randomly and the results are presented as the mean and standard deviation of these three measurements.

2.2. Preparation of ferrihydrite, adsorption complexes and coprecipitates

Two-line ferrihydrite (Fh) was prepared by dripping 1 M NaOH into a solution of 0.1 M FeCl$_3$ to reach a pH of 7.5 (Cornell and Schwertmann, 2003; Dublet et al., 2017). The procedure was performed rapidly (within 10 min) to avoid precipitation of akaganeite. Once the desirable pH was achieved and remained steady, the suspension was allowed to settle for three hours at 4 °C. Afterwards, the precipitate was centrifuged (4500g, 5 min), and the supernatant was discarded. After five Milli-Q water rinses, the resultant precipitate was resuspended in Milli-Q water to obtain a concentrated stock suspension, which was stored at 4 °C for use. Freshly synthesized Fh was used within 1 week for adsorption experiments. The remaining Fh was frozen in liquid nitrogen, freeze-dried and stored at 4 °C under dry conditions.

For adsorption experiments, 100 mL of Fh slurry (0.96 g L^{-1}) was mixed with 50 mL of EPS solution containing 48–1200 mg C L^{-1} under vigorous stirring in 10 mM NaCl background electrolyte. An electrolyte of 10 mM NaCl was chosen to facilitate comparison with previous work (Mikutta et al., 2007). The molar C/Fe ratios of these initial solutions were 0.2–5.0, and cover the range of molar C/Fe ratios found in soil pore water of paddy soils (Katoh et al., 2004), wetlands (Chin et al., 1998) and Fluvisol and Luvisol (Fritzsche et al., 2015). The pH of the adsorption experiments was set to 4.5 ± 0.1 by the dropwise addition of dilute NaOH and HCl. For coprecipitation experiments, 100 mL of FeCl$_3$·6H$_2$O solution (0.01 M) was added to pre-cleaned polyethylene bottles and mixed with 50 mL of EPS solution containing 48–1200 mg C L^{-1} under vigorous stirring in 10 mM NaCl background electrolyte. The molar C/Fe ratios of these initial solutions (0.2–5.0) were the same as in the adsorption experiments. The mixing of FeCl$_3$ and EPS was immediately followed by titration with freshly prepared 0.1 M NaOH at a rate of 97 mL min^{-1} until a pH of 3.6–3.8 was reached. The obtained solution was then slowly amended with NaOH until a final pH of 4.5 ± 0.1. This pH favours the formation of coprecipitates in the presence of dissolved OM (Eusterhues et al., 2011) and is close to the pH conditions regularly occurring in temperate and tropical soils (Wagai and Mayer, 2007). After 24 h of gently shaking the coprecipitation and adsorption suspensions end over end (90 rpm) at 20 °C in the dark (Omoike and Chorover, 2006; Chen et al., 2014), the suspensions were sedimented for 3 hours at 4 °C and the supernatants were carefully collected for analysis. The coprecipitates and adsorption complexes were then dialyzed (Spectrum, 3500 MWCO) at 4 °C in the dark until the electrical conductivity stabilized at ~20 µS cm^{-1}, in order to minimize structural changes and aggregation regularly caused by centrifugation. The Fh samples were then shock-frozen by dropwise injection of the suspension into liquid N$_2$, and subsequently freeze-dried. Shock-freezing of small volumes of mineral suspensions helps to reduce the effect of freeze-compaction caused by cryosuction (Hofmann et al., 2004). All EPS adsorption and coprecipitation experiments were performed in triplicate.

2.3. Element fractionation during adsorption and coprecipitation of EPS

To determine EPS-C, EPS-N and EPS-P sorption and element fractionation during adsorption and coprecipitation, the total organic C, N and P in the initial and post-sorption solutions were determined as above (Section 2.1), using a multi N/C 2100 analyzer (Analytik Jena, Jena, Germany) (for C and N) and via digestion with potassium peroxydisulfate (K$_2$S$_2$O$_8$) and measurement using the molybdenum blue spectrophotometric method (GB 11893-89) (for P). In addition, in order to study the bulk elemental compositions of the samples, the total C and N content of the adsorption complexes and coprecipitates were determined in an Elemental Analyser System (vario PYRO cube, Elementar, Germany). For determination of Fe content, ~5 mg of sample was dissolved in 2 mL of 36% HCl and diluted with 1% (v/v) HCl to a total volume of 25 mL. The Fe concentration was measured using an Agilent AA-240FS flame atomic absorption spectrophotometer (Agilent Technologies Inc., Santa Clara, CA, USA). For each elemental analysis a sub sample from each triplicate adsorption and coprecipitation experiment was chosen randomly and the results are presented as the mean and standard deviation of these three measurements.

2.4. Structural characterization of ferrihydrite, adsorption complexes and coprecipitates

X-ray diffraction (XRD) was used to verify the mineral phase of the synthesized Fh, adsorption complexes and coprecipitates. Diffractograms were obtained with a Bruker D8 ADVANCE diffractometer with θ-2θ geometry using Ni-filtered Cu-Kα radiation (λ = 0.15418 nm) (Bruker AXS Gmbh, Karlsruhe, Germany). The diffractometer was equipped with a LynxEye detector and operated at a tube voltage of 40 kV and a tube current of 40 mA. Scans were performed over the 2θ range of 5–80° with a step-size of 0.02° and scan rate of 10° min^{-1}. The microstructure images of selected freezed-dried samples were collected on a scanning electron microscope (SEM, Zeiss Merlin Compact, Germany) at 10.00 kV using a beam spot diameter of 20 µm. For XRD and SEM analyses a sub sample from each triplicate adsorption and coprecipitation experiment was chosen randomly and homogenized prior to measurement. The pH-dependent electrophoretic mobility (EM) of Fh, EPS, adsorption complexes and coprecipitates was measured in 10 mM NaCl background electrolyte with a Zetasizer Nano ZS Instrument (ZEN 3600, Malvern, UK) equipped with a 633-nm laser. The EM of the adsorption complexes and coprecipitates as a function of initial C/Fe molar ratios was also determined at pH 4.5. The zeta potential was obtained from the EM using the Smoluchowski equation (Sze et al., 2003). The particle size of Fh and colloid-sized aggregates at pH 4.5 in 10 mM NaCl was determined via static light scattering using the Zetasizer Nano ZS particle sizing unit. The uniform sphere model was applied. For EM and particle size measurements a sub sample from each triplicate adsorption and coprecipitation experiment was chosen randomly and homogenized

prior to measurement, then the average measurement was determined from 10 runs, with each run for EM including 12 cycles, and for particle size lasting for 60 s. The results are presented as the mean and standard deviation of these ten runs.

2.5. Fluorescence staining and confocal laser scanning microscopy (CLSM) analysis

Selected Fh-EPS associations were stained with fluorescent dyes using the protocol described previously (Zhang et al., 2015; Lin et al., 2016). Before staining, the associations were hydrated in 1.5 mL Eppendorf tubes with 0.1 M phosphate buffer saline (PBS) solution for 30 min in the dark. 4′,6-Diamidino-2-phenylindole dihydrochloride (DAPI) solution (0.1 mg mL^{-1}, 50 µL) was first added and stirred on a shaker table for 30 min at room temperature. Next, 0.1 M NaHCO$_3$ buffer (50 µL) was added to maintain the amine group in non-protonated form. Afterwards, SYPRO Orange protein gel stain (100× diluted stock solution, 20 µL) was added and incubated for 1 h. Finally, Concanavalin A (ConA) (0.25 mg mL^{-1}, 50 µL) was added and incubated for 30 min. After each of the above-mentioned three staining stages, the stained samples were washed three times with PBS to remove the extra stain and then stored at 4 °C before any observation. Confocal laser scanning microscopy (CLSM) (N-STORM, Nikon, Japan) was employed to visualize the distribution of nucleic acids, proteins and polysaccharides in Fh-EPS associations. These samples were imaged using a ×40 objective lens and processed using NIS-Elements Viewer software (version 4.50).

2.6. X-ray photoelectron spectroscopy (XPS) analysis

To obtain the distribution of elements at the sample near-surface (depth: 3–5 nm), XPS spectra of the freeze-dried unreacted EPS, Fh, adsorption complexes and coprecipitates were recorded using an ESCALAB 250Xi system (Thermo Scientific, United States). For XPS measurements a sub sample from each triplicate adsorption and coprecipitation experiment was chosen randomly and homogenized prior to measurement, and analyses were performed as point measurements with multiple (6–7) scans of each homogenized sample taken and averaged during software analysis using the Thermo Scientific TM Avantage Software (version 5.976). XPS of Fh was taken as a control. The measurements were carried out under vacuum, and used a monochromatic Al Ka X-ray source with a spot size of 500 µm. For survey spectra, the pass energy was set as 100 eV with a step size of 1.00 eV. In order to obtain C 1s high-resolution spectra, the pass energy was set as 30 eV with a step size of 0.05 eV. The atomic composition of the samples was estimated from integrating the core level peaks C 1s, N 1s, O 1s, P 2p and S 1s, using the Avantage Software. The atomic compositions are presented as the mean value and standard deviation of the several scans taken of each homogenized sample. The local chemical environment of C within the top few nanometers of the samples was determined with a least squares fitting scheme to deconvolve the high-resolution spectra, using the Avan-

tage Software. Before normalizing and fitting the high-resolution spectra to a Smart-type background, the charge-induced shift was calibrated by assigning the C1s peak to 284.8 eV. To specify different C oxidation states, the C 1s peak was split into four sub-peaks, as suggested by Omoike and Chorover (2004) and Poggenburg et al. (2018): (i) carbon displaying bonds to carbon and hydrogen in aliphatic and aromatic carbon (C—C, C=C, C—H; at 285.0 ± 0.1 eV), (ii) carbon displaying a single bond to oxygen or nitrogen in carbohydrates and amines (C—O, C—N; at 286.5 ± 0.2 eV), (iii) carbon displaying two bonds to oxygen in amides, aldehydes and ketones (C=O, O—C—O, O=C—N; at 288.0 ± 0.1 eV) and (iv) carbon displaying three bonds to oxygen in carboxylic carbon (O—C=O; at 289.1 ± 0.2 eV). Uncertainties on the atomic compositions and deconvolution results for C functional groups are those determined by the Avantage Software during the averaging and deconvolution fitting routine.

2.7. Carbon 1s near edge X-ray absorption fine structure (NEXAFS) analysis

To characterize the organic functional group chemistry, C 1s NEXAFS was performed using the soft X-ray spectroscopy beamline (4B7B) at the Beijing Synchrotron Radiation Facility (BSRF) (Beijing, China). A soft X-ray beam from the 2.5 GeV electron storage ring was produced, and a monochromator that was tunable over 1700–50 eV was illuminated by the beamline. For NEXAFS measurements a sub sample from each triplicate adsorption and coprecipitation experiment was chosen randomly and homogenized prior to measurement, and multiple scans of each homogenized sample were taken on randomly selected points and averaged. The homogenized sub samples were freeze-dried (∼10 mg) and mounted onto a gold-plated sample disc using double-sided adhesive Cu tape. The samples were measured in a vacuum under 10^{-6} Pa. The C 1s K-edge spectral signal was collected in total electron yield (TEY) mode and recorded over the energy range 280–310 eV with 0.05–0.5 eV step sizes. The smaller step size (0.05 eV) was selected at the energy level that can excite the core electron of carbon (283–293 eV). A dwell times of 1–1.5 ms were performed during stack measurements to avoid potential beam damage. The spot size of the beam was approximately 1.0 × 0.1 mm under the operating conditions. Background spectra were collected through the sample-free region of the Cu tape. The NEXAFS data were semi-quantitatively evaluated with a least squares fitting scheme to deconvolve the normalized spectra. An arctangent function was fixed at 290 eV to model the ionization step. The full width at half maximum of the bands was set as 0.4 ± 0.2 eV, and the amplitude was fluctuated during the fitting process. Spectral regions represented by Gaussian curves were described by attributing them to the functional groups G1 to G8. The positions of Gaussian curve components were confirmed by examining previously measured standard spectra (Kinyangi et al., 2006; Solomon et al., 2009), and the details assigned to specific functional groups are shown in Table A.2. Averaging, background subtraction, normalization and deconvolution of the NEXAFS spectra were

performed using the Athena program of the Demeter software package (version 0.9.26) (Ravel and Newville, 2005). Uncertainties on the deconvolution results for C functional groups are those determined by the Athena software during the deconvolution fitting routine.

2.8. Fourier transform infrared (FTIR) spectroscopy analysis

The freeze-dried EPS, Fh, adsorption complexes and coprecipitates were characterized by Fourier transform infrared spectroscopy (FTIR) on a Bruker Vertex 70 spectrometer (Bruker Optik GmbH, Ettlingen, Germany). For FTIR measurements a sub sample from each triplicate adsorption and coprecipitation experiment was chosen randomly and homogenized prior to measurement, and multiple scans of each homogenized sample were taken and averaged during software analysis using the OPUS software. The homogenized sub samples were mixed with KBr (spectroscopy grade) at a mass ratio of 1:100 and then pressed into discs with 13 mm diam. A total of 256 scans of each sub-sample were recorded from 4000 to 400 cm^{-1} at a resolution of 4 cm^{-1}. Spectral analysis was performed by using the OMNIC spectroscopy software (Thermo Scientific) and the identity of the spectral peaks was made by examining previously measured standard spectra summarized in Table A.3. An automatic baseline correction was applied to each spectrum before normalizing the summed absorbance from 4000 to 400 cm^{-1}. The normalized spectrum of pure ferrihydrite was subtracted from the spectra of the adsorption complexes and coprecipitates. To quantify relative changes in adsorbed and coprecipitated EPS, the selected spectral regions within the range of 1800–800 cm^{-1} are divided into the integrated peak areas of the following functional units: polysaccharide/organic P (1200–900 cm^{-1}), amide I (1750–1600 cm^{-1}), amide II (1600–1480 cm^{-1}) and carboxylate groups (1435–1375 cm^{-1}) (Fig. A.4).

2.9. Two-Dimensional Correlation Spectroscopy (2D-COS) analysis

After smoothing and baseline correction of the FTIR spectra, two-dimensional correlation (2D-COS) analysis of the adsorbed and coprecipitated EPS was applied to the FTIR spectra using the 2D-Shige software (version 1.3) (Kwansei-Gakuin University, Japan) (Noda and Ozaki, 2004; Schmidt and Martínez, 2016; Yan et al., 2016; Cai et al., 2018). The EPS concentration was used as the external perturbation. To illustrate this technique, an analytical spectrum $U(v, t)$ is considered, which is a function of a FTIR spectral variable v and a perturbation variable t. A discrete set of dynamic spectra measured at m points in time t between T_{min} and T_{max} can be expressed as:

$$U_j(v) = y(v, t_j) \qquad j = 1, 2, \ldots, m \tag{1}$$

while a set of dynamic spectra can be expressed as:

$$\widetilde{U}(v, t) = U(v, t_j) - \bar{U}(v) \tag{2}$$

where $\bar{U}(v)$ denotes the reference spectrum, which is typically the average spectrum and can be defined as:

$$\bar{U}(v) = \frac{1}{m} \sum_{j=1}^{m} U(v, t_j) \tag{3}$$

The discrete Hilbert–Noda transform is used to generate the synchronous Φ and asynchronous Ψ correlation intensities:

$$\Phi(v_1, v_2) = \frac{1}{m-1} \sum_{j=1}^{n} \widetilde{U}_j(v_1) \widetilde{U}_j(v_2) \tag{4}$$

$$\Psi(v_1, v_2) = \frac{1}{m-1} \sum_{j=1}^{m} \widetilde{U}_j(v_1) \sum_{k=1}^{m} M_{jk} \widetilde{U}_j(v_2) \tag{5}$$

where term M_{jk} corresponds to the jth column and the kth raw element of the discrete Hibert-Noda transformation matrix, and can be expressed as:

$$M_{jk} = \begin{cases} 0 & if \ j = k \\ \frac{1}{\pi(k-j)} & otherwise \end{cases} \tag{6}$$

The intensity of a synchronous correlation spectrum $\Phi(v_1, v_2)$ represents the simultaneous or coincidental changes of two separate spectral intensity variations measured at v_1 and v_2 during the time interval between T_{min} and T_{max} of the externally defined perturbation variable t. The intensity of an asynchronous correlation spectrum $\psi(v_1, v_2)$ represents sequential or successive, but not coincidental, changes of two separate spectral intensity variations measured at v_1 and v_2 during the time interval between T_{min} and T_{max} of the externally defined perturbation variable t.

The synchronous correlation spectrum $\Phi(v_1, v_2)$ contains autopeaks located at the diagonal line of the matrix (from the bottom left corner to the top right corner of the spectrum), and cross peaks located above the diagonal line (in the upper left region of the spectrum). Autopeaks represent the variation of the changes in the spectral intensities corresponding to the locations under the perturbation variable t. Cross peaks refer to the simultaneous changes of the spectral variables observed at two different locations (v_1 and v_2) under the perturbation variable t. Positive cross peaks indicate that the two variables (v_1 and v_2) change in the same direction, while negative cross peaks indicate that the two variables (v_1 and v_2) change in the opposite direction.

The asynchronous correlation spectrum $\psi(v_1, v_2)$ only shows cross peaks, which represent the sequence of the variable (v_1 and v_2) changes under the perturbation variable t. The rank order of intensity changes between two bands at v_1 and v_2 can be analyzed from the signs of the synchronous correlation peak $\Phi(v_1, v_2)$ and asynchronous correlation peak $\psi(v_1, v_2)$ based on previously established principles (Noda and Ozaki, 2004; Domínguez-Vidal et al., 2006; Jia et al., 2009). If $\Phi(v_1, v_2)$ and $\psi(v_1, v_2)$ have the same signs, the changes in the spectral intensity at band v_1 will occur prior to those at v_2; if they have opposite signs, the changes in the spectral intensity at band v_2 will occur prior to those at v_1. If $\psi(v_1, v_2)$ is zero then the changes at v_1 and v_2 will occur simultaneously (Noda and Ozaki, 2004; Domínguez-Vidal et al., 2006; Jia et al., 2009; Cai et al., 2018).

Here, because the spectral intensity changes reflect the sorption of the corresponding FTIR bands and thus the corresponding EPS functional groups, then the order in which the spectral intensity changes appear reflects the order in which the FTIR bands and thus the corresponding functional groups interact with Fh during adsorption and coprecipitation.

3. RESULTS

3.1. Bulk sorption and mass fractionation of EPS during adsorption and coprecipitation with ferrihydrite

The pure EPS extracted from *Bacillus subtilis* SBE1 is composed of carbon (340.8 ± 5.2 mg g^{-1}), nitrogen (58.8 ± 1.3 mg g^{-1}) and phosphorus (32.4 ± 1.1 mg g^{-1}) (Table A.1), resulting in C/N and C/P ratios of 5.8 and 10.5, respectively. Biochemical assays show a complicated mixture of biomacromolecules consisting primarily of polysaccharide (220.2 ± 9.4 mg g^{-1}) and protein (152.3 ± 6.5 mg g^{-1}), with small amount of nucleic acid (18.9 ± 0.9 mg g^{-1}) (Table A.1). The elemental content and biochemical composition of EPS extracted from *B. subtilis* SBE1 is similar to that of other *B. subtilis* (Mikutta et al., 2011) and has a similar protein content but lower polysaccharide content to that of other *B. subtilis* and *Pseudomonas putida* investigated using the same extraction method (Cao et al., 2011; Lin et al., 2016).

The sorption of EPS-C and EPS-N in both the adsorption and coprecipitation systems generally follows a Langmurian isotherm trend (Fig. 1a). At low molar C/Fe ratios, the amount of C and N sorbed in both the adsorption and coprecipitation systems increases with initial C/Fe ratio, and, except for the EPS-C coprecipitation system, reaches a maximum at higher C/Fe ratio. However, while the amount of EPS-N sorbed in both the adsorption and coprecipitation systems is similar, the amount of EPS-C sorbed in these two different EPS-Fh associations is higher than EPS-N. Furthermore, the amount of EPS-C sorbed is higher in the coprecipitation system (201.9 ± 6.0 mg g^{-1} at

C/Fe ratio of 5.0) compared to the adsorption system (118.7 ± 4.3 mg g^{-1} at C/Fe ratio of 5.0) (Fig. 1a; Table 1). At initial C/Fe ratio of 5.0, maximum EPS-C loading capacity, and perhaps maximum EPS-N loading capacity, in the coprecipitation system is not reached, and thus the loading capacity of the coprecipitates exceeds that of the adsorption complexes.

The C/N ratio of the sorbed EPS in both the adsorption systems (3.3–5.0) and coprecipitation systems (4.0–4.7) is lower than that of the unreacted EPS (5.8) and decreases with increasing C/Fe ratio (Fig. 1b; Table 1). The C/P ratio of the sorbed EPS estimated from the liquid phase shows a similar trend and decreases with increasing C/Fe ratio (Fig. A.1). The mass fraction of adsorbed EPS-C, -N and -P decreases with increasing C/Fe ratio compared to that for coprecipitated EPS-C, -N and -P, which maintains near complete EPS sorption even at C/Fe ratio of 5.0 (Fig. 2b; >0.85 mass fraction sorbed). A reduction in the sorbed EPS C/N and C/P ratios in both the adsorption and coprecipitation systems shows that the EPS is fractionated as a result of sorption, with an apparent selective retention of EPS-N and EPS-P over EPS-C. In particular, the mass fraction of adsorbed and coprecipitated EPS-P exceeds that of both EPS-N and EPS-C, except for the C/Fe ratio of 5.0 in the adsorption system (Fig. 2). EPS-P is thus disproportionately removed from the solutions relative to EPS-N and EPS-C, indicating a high affinity of EPS P-containing moieties with Fh during adsorption and coprecipitation. Overall these results show that EPS is selectively fractionated during adsorption to and coprecipitation with Fh, and that the selective fractionation of EPS elements resulting from adsorption is more pronounced than from coprecipitation.

3.2. Mineralogical and physiochemical characterization of adsorption complexes and coprecipitates

The pure Fh used for the adsorption systems exhibits two characteristically broad peaks at 0.26 nm (~34° 2θ) and 0.15 nm (~62° 2θ) (Fig. A.2). At comparably high
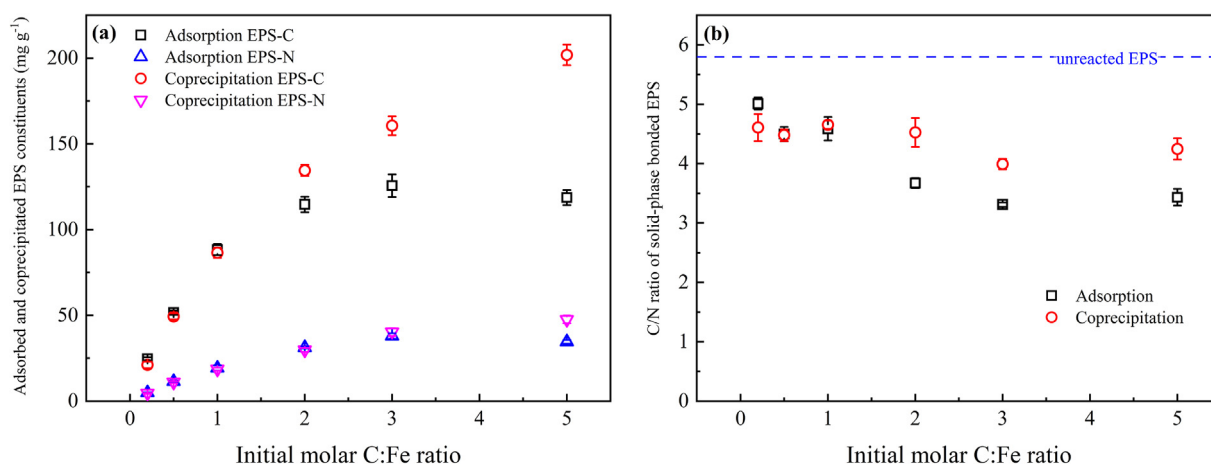

Fig. 1. EPS-C, -N contents (a) and C/N ratio (b) in the adsorption complexes and coprecipitates as a function of the initial molar C/Fe ratio. The dotted line shows the C/N ratio of unreacted EPS.

Table 1
Elemental composition, zeta potential and particle size of ferrihydrite, adsorption complexes and coprecipitates. Mean values ± standard deviations are calculated from a total of three measurements from triplicate samples (element) or ten measurements from a single homogenized sample (zeta potential, particle size).

Molar C/Fe ratios		contents				Zeta potential[c] (mV)	Particle size[d] (nm)
Initial	Of product	Fe (mg g^{-1})	C[a] (mg g^{-1})	N (mg g^{-1})	C/N[b]		
Ferrihydrite							
		565.6 ± 16.8				29.2 ± 1.2	639.2 ± 74.3
Adsorption complexes							
0.2	0.22	534.3 ± 26.8	24.7 ± 0.9	4.9 ± 0.1	5.0 ± 0.1	27.8 ± 1.0	776.8 ± 37.4
0.5	0.49	496.0 ± 26.1	51.6 ± 1.2	11.5 ± 0.6	4.5 ± 0.1	20.4 ± 1.1	1269.7 ± 39.4
1	0.93	442.2 ± 10.0	88.4 ± 3.2	19.3 ± 1.5	4.6 ± 0.2	9.1 ± 0.4	1481.8 ± 208.6
2	1.34	398.3 ± 7.9	114.7 ± 4.5	31.2 ± 0.6	3.7 ± 0.1	−11.4 ± 0.5	2185.2 ± 165.5
3	1.59	368.5 ± 23.7	125.6 ± 6.6	37.9 ± 1.6	3.3 ± 0.0	−21.3 ± 1.0	2427.2 ± 141.5
5	1.54	358.5 ± 6.9	118.7 ± 4.3	34.6 ± 1.1	3.4 ± 0.1	−25.6 ± 0.7	1786.4 ± 115.1
Coprecipitates							
0.2	0.21	480.1 ± 8.1	21.1 ± 1.9	4.6 ± 0.2	4.6 ± 0.2	41.3 ± 0.9	886.1 ± 57.4
0.5	0.54	426.1 ± 20.5	49.4 ± 1.8	11.0 ± 0.6	4.5 ± 0.1	32.4 ± 0.8	1006.0 ± 75.9
1	1.02	395.5 ± 27.7	86.0.5 ± 3.0	18.6 ± 0.9	4.7 ± 0.1	17.0 ± 0.9	1145.5 ± 100.3
2	1.98	317.5 ± 7.3	134.5 ± 3.2	29.8 ± 1.2	4.5 ± 0.2	10.9 ± 0.7	1759.3 ± 98.9
3	2.73	274.5 ± 2.3	160.6 ± 5.5	40.3 ± 2.2	4.0 ± 0.1	2.6 ± 0.9	2583.0 ± 96.7
5	4.07	231.6 ± 12.3	201.9 ± 6.0	47.6 ± 2.3	4.2 ± 0.2	−6.0 ± 0.7	2887.0 ± 195.9

[a] Corrected for the OC content of ferrihydrite (3.5 mg g^{-1}).
[b] The C/N of unreacted EPS is 5.8.
[c] Zeta potential determined at pH 4.5 in 10 mM NaCl.
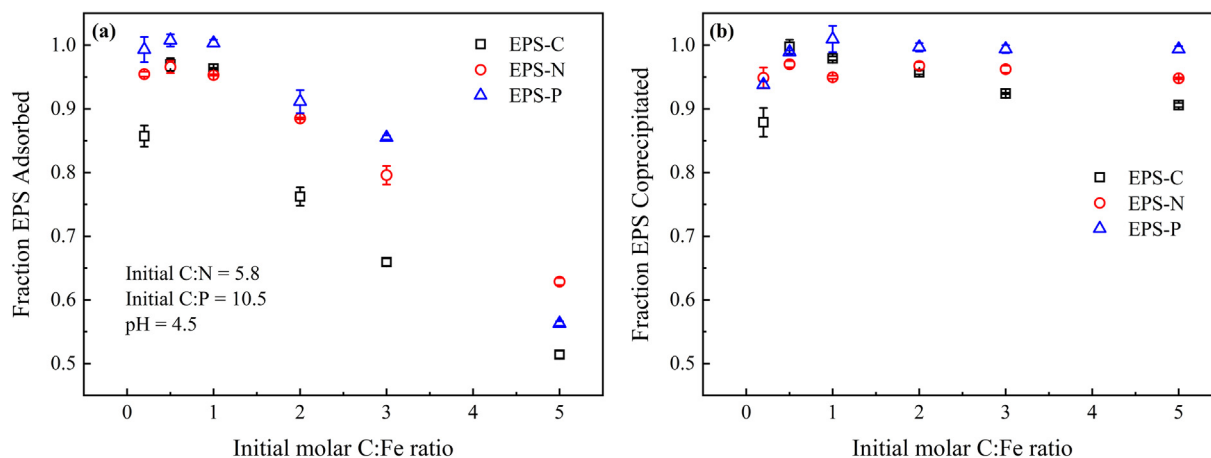[d] Particle size determined at pH 4.5 in 10 mM NaCl.

Fig. 2. The mass fraction of EPS-C, -N, -P adsorbed (a) and coprecipitated (b) as a function of the initial molar C/Fe ratio. Mass fraction of EPS-C, -N and -P sorbed is derived by calculating the ratio of the amount of EPS-C, -N and -P remaining in the supernatant to the amount of EPS-C, -N and -P added, and subtracting this ratio from 1.

C/Fe ratios, the XRD pattern of the adsorption complexes shows a relatively obvious additional peak (∼23° 2θ) than that of the coprecipitates, likely due to EPS diffraction in the low Bragg-angle region (Poggenburg et al., 2016). Adsorption and coprecipitation of EPS with Fh does not substantially change the XRD, but the two broad peaks are further broadened with increasing EPS loading, particularly for the coprecipitate samples up to C/Fe ratio of 5. Altogether, 2-line Fh is the dominant mineral phase in all complexes, which is observed in Fe(III) coprecipitates

formed in presence of exopolysaccharides, humic acid and natural OM (Mikutta et al., 2008; Chen et al., 2014; Mikutta et al., 2014).

The electrophoretic zeta potentials of the adsorption complexes and coprecipitates are lower than Fh and lie between Fh and EPS until pH exceeds 5, and decrease with increasing C/Fe ratio (Fig. 3; Table 1). The coprecipitates show higher zeta potential values than the adsorption complexes in the acidic and neutral pH range at equivalent C/ Fe ratios. The point of zero charge (PZC) of synthesized
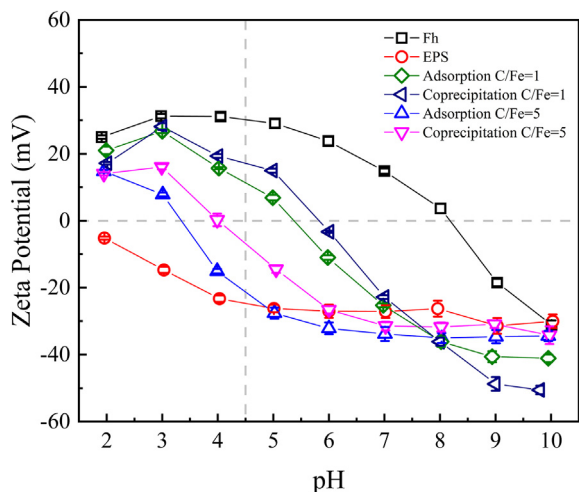
Fig. 3. Zeta potentials of Fh, EPS, adsorption complexes and coprecipitates as a function of pH. Zeta potentials were determined in 10 mmol L^{-1} NaCl at solid concentrations of 0.5 g L^{-1}. Initial molar C/Fe ratios of selected adsorption complexes and coprecipitates used for zeta potential measurements were 1 and 5, respectively.

pure Fh is located at pH 8.2, which is consistent with previous study results (Cornell and Schwertmann, 2003).

The adsorption complexes and coprecipitates exhibit larger average particle sizes than the pure Fh (~639 nm) (Table 1). Adsorption results in an increase in average particle size similar to coprecipitation at low C/Fe ratio, followed by a decrease at C/Fe ratio of 5. However, coprecipitation results in continuously increasing average particle size from 886 to 2887 nm with increasing C/Fe ratios. Inhibition of larger particle formation in the adsorption complexes at high C/Fe ratio likely results from a steric effect in which residual EPS in solution retards the growth of Fh particles that are coated in EPS, rather than incorporating EPS (Lin et al., 2018). Overall these results show that the physiochemical properties of EPS-Fh associations are affected by the EPS-Fh formation pathways.

3.3. Morphology and distribution of EPS on adsorption complexes and coprecipitates

The SEM results show that pure Fh, adsorption complex and coprecipitate with C/Fe ratio of 5 are all comprised of irregular Fh nanoparticles clustered into small aggregates (Fig. 4, top panel). The CLSM images show the distribution plots of proteins, polysaccharides and nucleic acids on pure Fh, adsorption complex and coprecipitate after fluorescent staining (Fig. 4, bottom panel; note in Fig. 4a that Fh does not cause spontaneous fluorescence interference). Nucleic acids and proteins are the predominant EPS components distributed on the surfaces of the adsorption complex particles at C/Fe ratio of 5, with a minor distribution of polysaccharides (Fig. A.3), however, polysaccharides show a patchy distribution on the surfaces of the coprecipitate particles at C/Fe ratio of 5. In agreement with the mass fractionation results, CLSM therefore also shows that different EPS components are retained to varying degrees with the adsorption and coprecipitation particles.

3.4. Surface element contents and carbon speciation of adsorption complexes and coprecipitates

3.4.1. XPS analysis of EPS-ferrihydrite associations

To gain further insight into the mass fractionation of EPS during adsorption and coprecipitation with Fh, XPS analysis is used to probe the distribution of major elements on the near surfaces of individual samples (Table 2). Quantitative measurement of XPS spectra of unreacted EPS detect 57.07 ± 0.10 atom% C, 8.63 ± 0.08 atom% N, 2.51 ± 0.02 atom% P, resulting in near surface EPS C/N and C/P atomic ratios of 6.6 and 22.7, respectively. The near surface EPS C/N ratio is similar to the bulk EPS C/N ratio (5.8). However, the near surface EPS C/P ratio is higher than the bulk EPS C/P ratio (10.5). This is also reported for EPS adsorbed to and coprecipitated with Al (hydr)oxides (Mikutta et al., 2011) and is likely attributable to the low atom% P content exacerbating the effect of surface adventitious carbon. For adsorption complexes at C/Fe ratio of 5, the near surface C/N ratio of adsorbed EPS is slightly decreased (by <2) while the near surface C/P ratio of adsorbed EPS is markedly decreased (by >8) compared to the unreacted EPS. This shows there is selective adsorption of N-containing and P-containing biomolecules at the near surface of the adsorption complexes, in agreement with the mass fractionation results. Interestingly, the near surface C/N and C/P ratios of the coprecipitated EPS are higher than those of the unreacted EPS, which is contrary to the mass fractionation results shown by the bulk C/N and C/P ratio trends. This points towards relative enrichment of C-containing biomolecules at the near surface of the coprecipitates. In adsorption complexes produced at C/Fe ratio of 1 and 5, the near surface C/(Fe + C) molar ratio is considerably higher than the bulk C/(Fe + C) ratio. This is manifest in the near surface to bulk C/(Fe + C) ratio ranging from 1.90 (C/Fe ratio 1) to 1.54 (C/Fe ratio 5) (Table 2), thus indicating that C is mainly located on the surface of the adsorption complexes. In coprecipitates produced at C/Fe ratio of 1 and 5, the near surface to bulk C/(Fe + C) ratio is reduced compared to the adsorption complexes, ranging from 1.85 (C/Fe ratio 1) to 1.22 (C/Fe ratio 5), thus indicating that C and Fe are relatively more homogeneously distributed in coprecipitates formed at high C/Fe ratio (>1 in this study). When the C/Fe ratio is less than 1, the near surface to bulk C/(Fe + C) ratio of the coprecipitates are more similar to those of the adsorption complexes, suggesting that low EPS-C concentration in the coprecipitation system likely decreases the involvement of EPS in the aggregation of Fh, leading to the distribution of some EPS-C on the surface of the newly-formed Fh particles.

XPS analysis also provides insights into the local chemical environment of C within the top few nanometers of the sample particles. Detailed C 1s XPS spectra of the near surface of freeze-dried EPS, adsorption complexes and coprecipitates are deconvoluted into four spectral regions
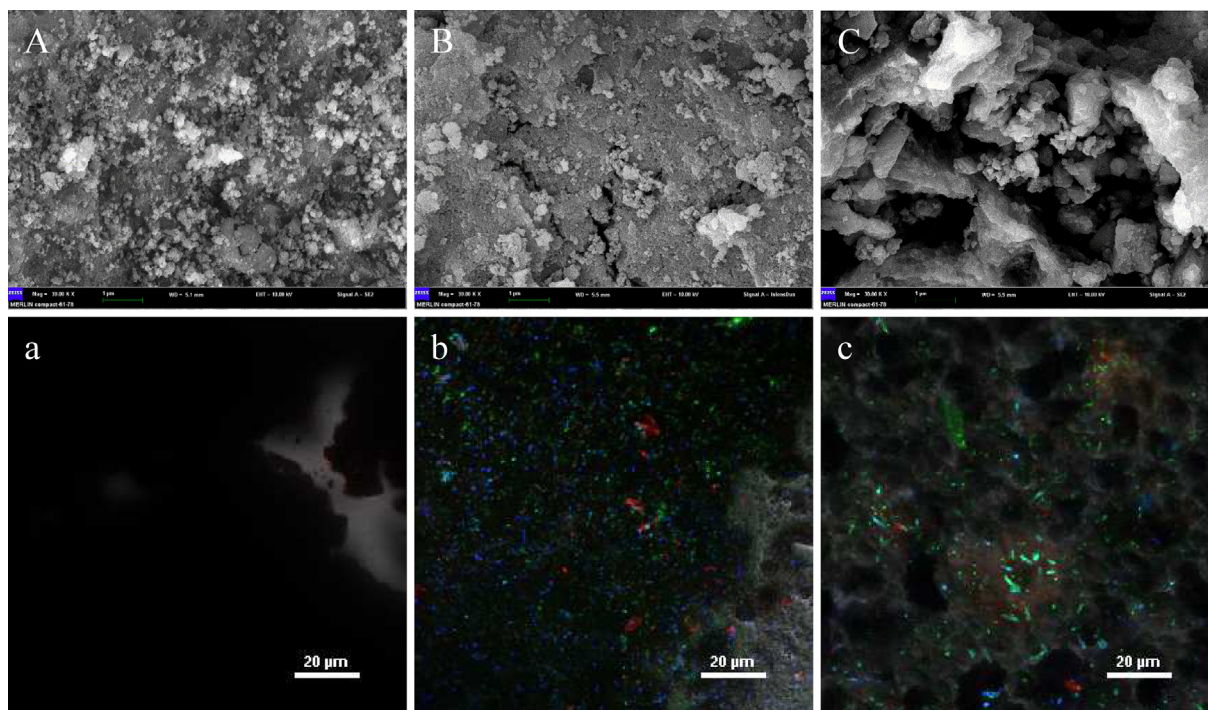
Fig. 4. The visual images of ferrihydrite, adsorption complexes and coprecipitates. (A) SEM image and (a) CLSM image of pure ferrihydrite; (B) SEM image and (b) CLSM image of adsorption complex with an initial molar C/Fe ratio of 5; (C) SEM image and (c) CLSM image of coprecipitate with an initial molar C/Fe ratio of 5. Colour allocation of CLSM images: blue (DAPI) nucleic acids; green (SYPRO Orange) proteins; red (ConA) α-polysaccharides. Scale bars of SEM and CLSM images are 1 and 20 μm, respectively.

(Omoike and Chorover, 2004; Poggenburg et al., 2018a). The near surface of unreacted EPS is mainly composed of carbohydrate C ($43.6 \pm 0.18\%$), aliphatic C ($34.4 \pm 0.07\%$) and amide C ($18.9 \pm 0.92\%$), with a small proportion of carboxylic C ($3.1 \pm 0.8\%$) (Fig. 5). Adsorption and coprecipitation reactions alter the chemical composition of near surface-bound EPS. The relative proportions of aliphatic C on the near surface of the adsorption complexes ($36.1 \pm 0.08\%$ – $42.2 \pm 0.16\%$) and coprecipitates ($40.1 \pm 0.09\%$ – $45.4 \pm 0.55\%$) are higher than those of unreacted EPS. These results show that aliphatic C present in proteins and phospholipids is preferentially adsorbed and coprecipitated. Although sorptive fractionation causes a decrease in carbohydrate C compared with unreacted EPS, the sorbed EPS still has a high proportion of carbohydrate C in the adsorption complexes ($36.0 \pm 0.15\%$ – $40.3 \pm 0.15\%$) and coprecipitates ($35.4 \pm 0.23\%$ – $39.4 \pm 0.53\%$) (Fig. 5). At C/Fe ratio ≥ 1, compared with the unreacted EPS, the relative proportion of amide C is increased in the adsorption complexes ($22.1 \pm 0.68\%$ – $24.9 \pm 0.12\%$) and decreased in the coprecipitates ($17.0 \pm 0.28\%$ – $18.5 \pm 0.45\%$) (Fig. 5), and thus amide C present in proteins is preferentially adsorbed to the surface of Fh, consistent with the decreased near surface C/N ratio.

3.4.2. Carbon 1s NEXAFS analysis of EPS-ferrihydrite associations

The C 1s NEXAFS spectra of all samples display roughly similar C signals containing two distinct peaks at 285.4 and 288.5 eV (Fig. 6). According to literature reference spectra, the peak at 285.4 eV is attributable to aromatic functional groups, and the slightly broadened peak at 288.5 eV is attributable to both carboxylic ($\sim$288.6 eV) and amide (288.2 eV) functional groups (Lawrence et al., 2003; Kinyangi et al., 2006; Chan et al., 2009; Li et al., 2016). Deconvolution results reveal that at C/Fe ratio ≥ 1, compared with the unreacted EPS ($31.84 \pm 1.37\%$), the relative proportion of carboxylic/amide C is generally increased in the adsorption complexes ($32.96 \pm 1.01\%$ – $47.98 \pm 1.65\%$) and somewhat decreased in the coprecipitates ($28.57 \pm 0.79\%$ – $30.86 \pm 0.83\%$) (Table 3), which is consistent with the preferential association of acidic polysaccharides and proteins with the adsorption complexes shown by XPS. Retention of acidic polysaccharides is also consistent with the lower zeta potential values of the adsorption complexes compared to the coprecipitates at equivalent C/Fe ratios. Based on the deconvolution results, four additional peaks are also semiquantitatively identified. When the C/Fe ratio increases from 1, the relative proportions of aliphatic C and O-alkyl C in the coprecipitates ($29.43 \pm 0.66\%$ – $31.21 \pm 0.36\%$ and $27.30 \pm 0.96\%$ – $32.39 \pm 0.55\%$, respectively) are generally higher than those of the adsorption complexes ($14.51 \pm 0.44\%$ – $27.50 \pm 0.73\%$ and $26.94 \pm 0.72\%$ – $27.98 \pm 0.93\%$, respectively), indicating that more lipids and polysaccharide components are retained in the coprecipitates, consistent with the results of EPS visualization by CLSM.

Table 2
Surface element composition of freeze-dried EPS, adsorption complexes and coprecipitates revealed by XPS. Mean values ± standard deviations are shown for the analysis results of at least six XPS scans of a single homogenized sample.

Initial molar C/Fe ratio	O^a atomic %	S^a	C^a	N^a	P^a	Fe^a	C/N	C/P	C/Fe	$Surface_{C/(Fe+C)}$/$Bulk_{C/(Fe+C)}$[b]
EPS										
	31.42 ± 0.06	0.13 ± 0.06	57.07 ± 0.10	8.63 ± 0.08	2.51 ± 0.02	0.24 ± 0.02	6.61 ± 0.07	22.74 ± 0.22		
Adsorption										
0.2	49.96 ± 0.13	0.35 ± 0.12	25.11 ± 0.11	2.49 ± 0.04	0.86 ± 0.10	21.24 ± 0.28	10.10 ± 0.13	29.33 ± 3.18	1.18 ± 0.02	4.78
0.5	47.81 ± 0.45	0.24 ± 0.05	31.65 ± 0.51	4.04 ± 0.02	1.11 ± 0.12	15.15 ± 0.22	7.84 ± 0.17	28.79 ± 2.67	2.09 ± 0.06	2.78
1	44.79 ± 0.13	0.20 ± 0.03	33.24 ± 0.11	5.61 ± 0.08	1.71 ± 0.12	14.44 ± 0.05	5.92 ± 0.09	19.54 ± 1.37	2.30 ± 0.01	1.90
2	41.62 ± 0.16	0.30 ± 0.14	36.18 ± 0.05	7.41 ± 0.02	2.19 ± 0.06	12.30 ± 0.05	4.88 ± 0.02	16.53 ± 0.47	2.94 ± 0.02	1.63
3	41.46 ± 0.44	0.24 ± 0.10	38.21 ± 0.17	8.06 ± 0.06	2.40 ± 0.06	9.64 ± 0.12	4.74 ± 0.04	15.95 ± 0.38	3.96 ± 0.04	1.54
5	41.80 ± 0.17	0.20 ± 0.03	35.97 ± 0.16	7.76 ± 0.03	2.68 ± 0.03	11.59 ± 0.05	4.64 ± 0.04	13.42 ± 0.10	3.10 ± 0.03	1.54
Coprecipitation										
0.2	49.89 ± 0.39	0.35 ± 0.11	24.42 ± 0.27	1.90 ± 0.08	0.74 ± 0.23	22.70 ± 0.27	12.84 ± 0.43	35.03 ± 9.30	1.08 ± 0.02	4.90
0.5	46.66 ± 0.55	0.26 ± 0.08	33.86 ± 0.59	3.21 ± 0.03	0.97 ± 0.12	15.05 ± 0.26	10.55 ± 0.25	35.34 ± 3.76	2.24 ± 0.08	2.60
1	42.43 ± 0.26	0.30 ± 0.12	38.02 ± 0.05	4.96 ± 0.14	1.32 ± 0.12	12.96 ± 0.05	7.68 ± 0.22	28.90 ± 2.69	2.93 ± 0.01	1.85
2	38.69 ± 0.20	0.21 ± 0.03	43.22 ± 0.09	6.40 ± 0.02	1.87 ± 0.03	9.61 ± 0.02	6.75 ± 0.01	23.16 ± 0.31	4.50 ± 0.01	1.44
3	36.92 ± 0.18	0.17 ± 0.02	47.06 ± 0.06	7.21 ± 0.08	1.94 ± 0.08	6.70 ± 0.02	6.53 ± 0.07	24.32 ± 0.94	7.02 ± 0.02	1.33
5	34.45 ± 0.19	0.26 ± 0.06	49.25 ± 0.10	8.34 ± 0.01	2.45 ± 0.05	5.25 ± 0.02	5.90 ± 0.01	20.08 ± 0.39	9.39 ± 0.02	1.22

[a] Corrected for traces of Na and Cl.
[b] $Surface_{C/(Fe+C)}$/$Bulk_{C/(Fe+C)}$ = the ratio of surface to bulk C/(C + Fe) molar ratio.
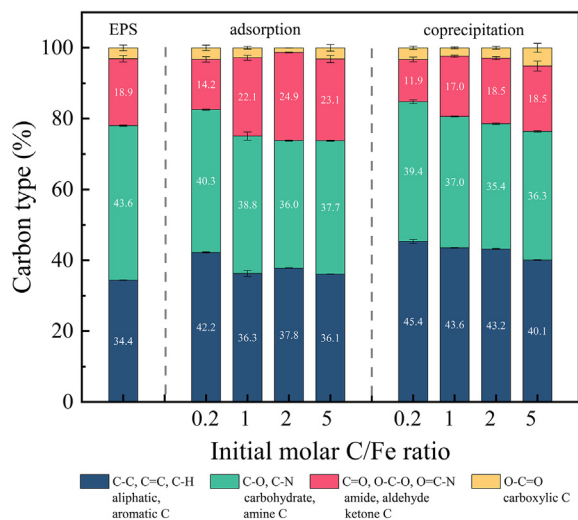
Fig. 5. Distribution of different carbon species in freeze-dried EPS, adsorption complexes and coprecipitates derived from detailed XPS C 1s measurements.

3.5. Interaction of EPS functional groups during adsorption and coprecipitation with ferrihydrite

3.5.1. FTIR spectroscopy of EPS-ferrihydrite associations

The FTIR spectrum of pure EPS exhibits broad signals consisting of vibrations of amide bonds in proteins (amide I, 1653 cm^{-1}), deformation vibrations of N-H and valence vibrations of C-N in —CO—NH— of proteins (amide II, 1552 cm^{-1}), symmetric C-O vibrations of carboxylic groups in complexes (1405 cm^{-1}) and overlapping C-O stretching vibrations of polysaccharides as well as symmetric stretching vibrations of P=O in the phosphodiester backbone of nucleic acids (1084 cm^{-1}) (Fig. A.4; Table A.3). The FTIR spectra of adsorbed and coprecipitated EPS are altered in several regions, compared with those of unreacted EPS, indicating selective sorption of particular EPS moieties in

agreement with the mass fractionation, XPS and NEXAFS results. Most important is the emergence of a new band, located at ~1004 cm^{-1} (Fig. A.4), that is consistent with stretching vibrations of P—O—Fe bonds as reported in prior studies (Omoike and Chorover, 2006). As initial molar C/Fe ratio increases, the peak area ratios of the amide I/amide II peak in the coprecipitates increase from 1.00 to 1.33, while the peak area ratios in the adsorption complexes are higher (between 1.26 and 1.54) and more similar to those of the unreacted EPS (1.53) (Table 4). This phenomenon shows that there is preferential sorption of amide II into coprecipitates. With increasing C/Fe ratio, the peak area ratios of carboxylate/amide (I + II) in adsorbed and coprecipitated EPS decrease from 0.15 to 0.08 and from 0.17 to 0.09, respectively, relative to 0.07 in unreacted EPS, indicating that carboxylic groups are more important for adsorption and coprecipitation of EPS at low molar C/Fe ratios. At equivalent C/Fe ratios the peak area ratios of amide (I + II)/(polysaccharide + nucleic acids) in coprecipitated EPS (between 1.08 and 1.91) are higher than those in adsorbed EPS (between 0.87 and 1.79), indicating that polysaccharides and organic P components are relatively less retained than protein components in the coprecipitates, which is inconsistent with the mass fractionation, XPS and NEXFAS results. This inconsistency may be due to some overlap of the phosphate band and polysaccharide vibrations such that it is difficult to properly distinguish the two, together with an interference of newly formed P—O—Fe bonds on this peak area (1200–900 cm^{-1}), as mentioned by Omoike and Chorover (2006).

3.5.2. 2D-COS analysis of the interaction between EPS and ferrihydrite

To enhance the spectral resolution and further explore the detailed sorption mechanisms of EPS adsorbed and coprecipitated with Fh, 2D-COS analysis is conducted on the FTIR spectra (Fig. 7). The synchronous maps exhibit seven characteristic autopeaks at 1658, 1544, 1408, 1246,
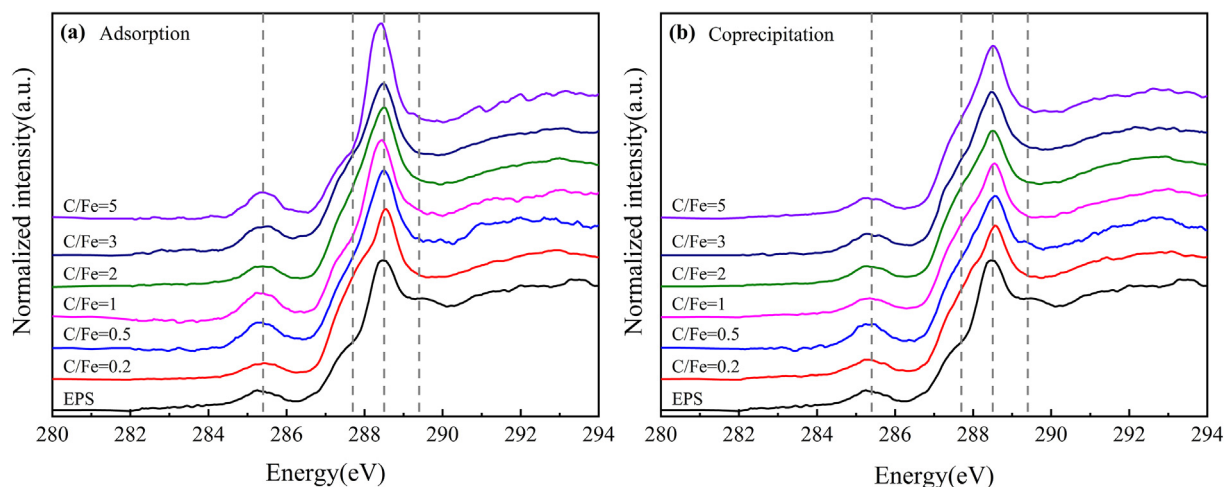

Fig. 6. C 1s NEXAFS spectra of adsorption complexes (a) and coprecipitates (b) at different molar C/Fe ratios compared to the original unreacted EPS. Numbers on the left of the spectra indicate the initial molar C/Fe ratios.

Table 3
Deconvolution results for organic groups in EPS, adsorption complexes and coprecipitates using C 1s NEXAFS. Mean values ± standard deviations are shown for the deconvolution results of at least three NEXAFS scans of a single homogenized sample.

Initial molar C/Fe ratio	Proportion of sorption regions (%)					
	Aromatic C 283.0–286.2 eV G1 + G2 + G3	Phenolic C 286.0–287.4 eV G4	Aliphatic C 287.0–287.6 eV G5	Carboxylic/Amide C 288.0–288.7 eV G6	O-alkyl C 289.2–289.5 eV G7	Carbonyl C 289.5–290.3 eV G8
EPS						
	7.18 ± 0.13	0.16 ± 0.01	25.52 ± 0.60	31.84 ± 1.37	30.32 ± 0.53	4.97 ± 0.09
Adsorption						
0.2	3.95 ± 0.09	0.42 ± 0.03	31.33 ± 1.26	31.90 ± 1.44	28.83 ± 1.41	3.57 ± 0.17
0.5	7.12 ± 0.18	0.53 ± 0.01	26.04 ± 1.03	34.40 ± 1.46	24.23 ± 0.86	7.69 ± 0.22
1	6.20 ± 0.21	0.34 ± 0.01	16.17 ± 0.65	44.85 ± 1.51	27.20 ± 0.66	5.25 ± 0.01
2	6.65 ± 0.26	0.14 ± 0.01	23.52 ± 0.31	39.09 ± 0.97	27.46 ± 0.97	3.14 ± 0.04
3	9.56 ± 0.19	0.63 ± 0.02	27.50 ± 0.73	32.96 ± 1.01	26.94 ± 0.72	2.42 ± 0.00
5	7.00 ± 0.22	0.83 ± 0.03	14.51 ± 0.44	47.98 ± 1.65	27.98 ± 0.93	1.70 ± 0.07
Coprecipitation						
0.2	6.76 ± 0.13	1.30 ± 0.08	27.06 ± 0.35	34.29 ± 1.30	24.58 ± 0.51	6.01 ± 0.27
0.5	6.61 ± 0.18	0.52 ± 0.04	29.06 ± 0.28	29.99 ± 0.88	31.88 ± 0.62	1.93 ± 0.05
1	6.52 ± 0.09	0.60 ± 0.05	30.34 ± 0.34	28.57 ± 0.79	32.39 ± 0.55	1.57 ± 0.06
2	6.71 ± 0.12	0.08 ± 0.01	31.21 ± 0.36	28.88 ± 1.00	28.65 ± 0.89	4.46 ± 0.17
3	6.44 ± 0.16	0.40 ± 0.02	29.93 ± 0.45	29.97 ± 0.55	27.30 ± 0.96	5.96 ± 0.26
5	6.34 ± 0.18	0.39 ± 0.02	29.43 ± 0.66	30.86 ± 0.83	27.71 ± 0.75	5.26 ± 0.37

1140, 1078 and 998 cm^{-1} for adsorption, and five characteristic autopeaks at 1658, 1544, 1408, 1072 and 1006 cm^{-1} for coprecipitation. These autopeaks are assigned to the amide I (1658 cm^{-1}), amide II (1544 cm^{-1}), carboxylate C=O (1408 cm^{-1}), P=O asymmetric stretch (1246 cm^{-1}), C—O ring vibration (1140 cm^{-1}), nucleic acid P=O/polysaccharide C—O—C (1078; 1072 cm^{-1}) and P—O—Fe bonds (1006; 998 cm^{-1}) (Table A.3). The band corresponding to the nucleic acid P=O is overlapping with the polysaccharide C—O—C in the synchronous maps, presenting only one broad peak at 1078 or 1072 cm^{-1}. The intensities of the autopeaks located at the diagonal line of the synchronous maps (from the bottom left corner to the top right corner of the maps) can represent the overall susceptibility of the corresponding spectral region to changes in spectral intensity as an external perturbation variable, in this case increasing EPS concentration, is applied to the system. In this study, the intensities of the autopeaks follow the order: 1658 > 1544 > 998 > 1078 > 1140 > 1408 > 1246 cm^{-1} for adsorption, and 1658 > 1544 > 1072 > 1006 > 1408 cm^{-1} for coprecipitation, and thus show that the relative sorption intensity of the amide functional groups during adsorption and coprecipitation is greater than that of the other functional groups (Fig. 7a and c). Because the relative sorption intensity of a functional group is related to the amount sorbed of that functional group, then in turn, these results indicate that more amide groups are sorbed than other functional groups in adsorption and coprecipitation reactions. These results also confirm that more EPS molecules related to polysaccharide C-O-C are coprecipitated with Fe species than adsorbed to Fh. The cross peaks above the diagonal line of the synchronous maps (in the upper left region of the maps) display positive signs (Fig. 7a and c, Table A.4), suggesting that the in-phase variations among

the corresponding functional groups are correlated with the amount of EPS sorbed.

The sign of the cross peaks of the synchronous maps compared to the asynchronous maps reveals the rank order of sorption of the corresponding spectral regions and thus the corresponding functional groups. To illustrate this we add an exemplary label (1544/1078 or 1544/1072) to Fig. 7, where the locations of 1544/1078 (for the adsorption samples) or 1544/1072 (for the coprecipitation samples) represent the cross peaks between amide II (1544 cm^{-1}) and nucleic acid P=O/polysaccharide C—O—C (1078; 1072 cm^{-1}). The rank order of sorption of amide II and nucleic acid P=O/polysaccharide C—O—C can be determined from the signs of the synchronous (1544/1078 or 1072) and asynchronous (1544/1087 or 1072) cross peaks, where if the cross peaks have the same signs then the sorption of band 1544 cm^{-1} will occur before band 1078/1072 cm^{-1}, whereas if the cross peaks have opposite signs then the sorption of band 1078/1072 cm^{-1} will occur before band 1544 cm^{-1} (Noda and Ozaki, 2004; Domínguez-Vidal et al., 2006; Jia et al., 2009). For the adsorption complexes the signs of the cross peak 1544/1078 in the synchronous and asynchronous (in the brackets) maps are + (−), and thus sorption occurs in the order of 1078 → 1544 cm^{-1}, indicating that the bonding sequence of EPS adsorption to ferrihydrite is: nucleic acid P=O/polysaccharide C—O—C > amide II. For the coprecipitates the signs of the cross peak 1544/1072 in the synchronous and asynchronous (in the brackets) maps are + (+), and thus sorption occurs in order of 1544 → 1072 cm^{-1}, indicating that the bonding sequence of EPS coprecipitation with Fe species is: amide II > nucleic acid P=O/polysaccharide C—O—C.

Following this application of Noda's rule (Noda and Ozaki, 2004), adsorption occurs in the order of 1246 → 1078 → 1408 → 1140 → 1658, 1544 → 998 cm^{-1}, indicating

Table 4
Qualitative assessment of FTIR spectra of adsorbed and coprecipitated EPS at various initial molar C/Fe ratios.

Functional unit	IR region (cm⁻¹)	Unreacted EPS	Initial molar C/Fe ratio of adsorption complexes						Initial molar C/Fe ratio of coprecipitates					
			0.2	0.5	1	2	3	5	0.2	0.5	1	2	3	5
Integrated peak areas (a.u.)														
COO⁻	1434–1374	8.36	2.45	4.25	5.93	7.23	6.73	6.62	2.05	3.81	7.07	8.27	8.63	9.84
Amide I	1750–1600	70.69	8.99	24.10	31.75	47.32	46.38	49.51	6.04	14.58	30.22	44.43	53.81	64.47
Amide II	1600–1480	46.20	7.11	16.68	21.18	32.20	30.16	33.94	6.05	13.57	27.74	37.67	42.12	48.64
Amide I + II	1750–1480	116.89	16.11	40.78	52.93	79.52	76.55	83.45	12.09	28.14	57.96	82.10	95.93	113.11
Poly[a] + nucleic acids	1200–940	49.31	18.51	31.64	41.18	44.51	45.19	49.58	11.20	25.46	30.37	42.88	50.79	65.11
Peak area ratios														
COO⁻/amide I		0.12	0.27	0.18	0.19	0.15	0.15	0.13	0.34	0.26	0.23	0.19	0.16	0.15
COO⁻/amide I + II		0.07	0.15	0.10	0.11	0.09	0.09	0.08	0.17	0.14	0.12	0.10	0.09	0.09
COO⁻/Poly		0.17	0.13	0.13	0.14	0.16	0.15	0.13	0.18	0.15	0.23	0.19	0.17	0.15
Amide I/amide II		1.53	1.26	1.44	1.50	1.47	1.54	1.46	1.00	1.07	1.09	1.18	1.28	1.33
Amide I/Poly		1.43	0.49	0.76	0.77	1.06	1.03	1.00	0.54	0.57	1.00	1.04	1.06	0.99
Amide II/Poly		0.94	0.38	0.53	0.51	0.72	0.67	0.68	0.54	0.53	0.91	0.88	0.83	0.75
Amide I + II/Poly		2.37	0.87	1.29	1.29	1.79	1.69	1.68	1.08	1.11	1.91	1.91	1.89	1.74

[a] Poly, polysaccharide components.

that the full bonding sequence of EPS adsorption to ferrihydrite is: P=O asymmetric stretch > nucleic acid P=O/polysaccharide C—O—C > carboxylate C=O > C—O ring vibration > amide I, amide II > P—O—Fe bonds (Table A.4). Coprecipitation occurs in order of 1408 → 1544 → 1658 → 1072 → 1006 cm⁻¹, indicating that the full bonding sequence of EPS coprecipitation with Fe species is: carboxylate C=O > amide II > amide I > nucleic acid P=O/polysaccharide C—O—C > P—O—Fe bonds (Table A.4). Overall, in the two formation pathways, the chemical complexation of carboxylate functional groups in the reaction of EPS with Fh occurs prior to that of amide functional groups. During adsorption to Fh however, the P=O functional groups are sorbed faster than the carboxylate and amide functional groups, while during coprecipitation the P=O functional groups are sorbed slower than the carboxylate and amide functional groups.

The other asynchronous cross peaks at (1624, 1544), (1674, 1624), (1622, 1544), (1695, 1544), and (1695, 1651) are not identified in the synchronous maps of the adsorption and coprecipitation samples, and so the rank order of sorption of the corresponding spectral regions and thus the corresponding functional groups cannot be determined. The same observation is also reported in a previous study using 2D-COS, and might be attributable to bandwidth change or peak position shift in spectra during reactions (Noda, 2017). Despite this, the appearance of these asynchronous cross peaks indicates that the relative proportions of these secondary structural components changes at different rates during the different (adsorption and coprecipitation) sorption reactions. In addition, the asynchronous map reveals that the peak at 1078 cm⁻¹ existing in the one-dimensional infrared spectra is overlapping with the peaks at 1087 and 1045 cm⁻¹, and that the peak at 1072 cm⁻¹ in the one-dimensional infrared spectra is overlapping with the peaks at 1102 and 1056 cm⁻¹. As such 2D-COS asynchronous maps can capture the subtle response of the EPS structure during interactions with Fh.

4. DISCUSSION

4.1. EPS adsorption versus coprecipitation with ferrihydrite

EPS represents a mixture of biomolecules containing a diversity of functional groups that govern EPS interactions with Fe (oxyhydr)oxides. Previous work shows that heterogeneous EPS can react with a preexisting Fe (oxyhydr)oxide sorbent to form a variety of organomineral chemical bonds of varying strength (Omoike and Chorover, 2006; Liu et al., 2013; Poggenburg et al., 2018b). In contrast, coprecipitation of EPS with Fe (oxyhydr)oxide results in both adsorption and occlusion of EPS molecules in the interstices between the ferrihydrite crystals (Eusterhues et al., 2011), and thus involves both chemical and physiochemical interaction processes (Kleber et al., 2015). Here, at high C/Fe ratios (>1) and pH 4.5, substantially more organic carbon is taken up during coprecipitation than during adsorption, likely due to a greater accessibility of monomeric Fe species to EPS functional groups during the coprecipitation process (Fig. 1a; Table 1). This agrees with previous suggestions
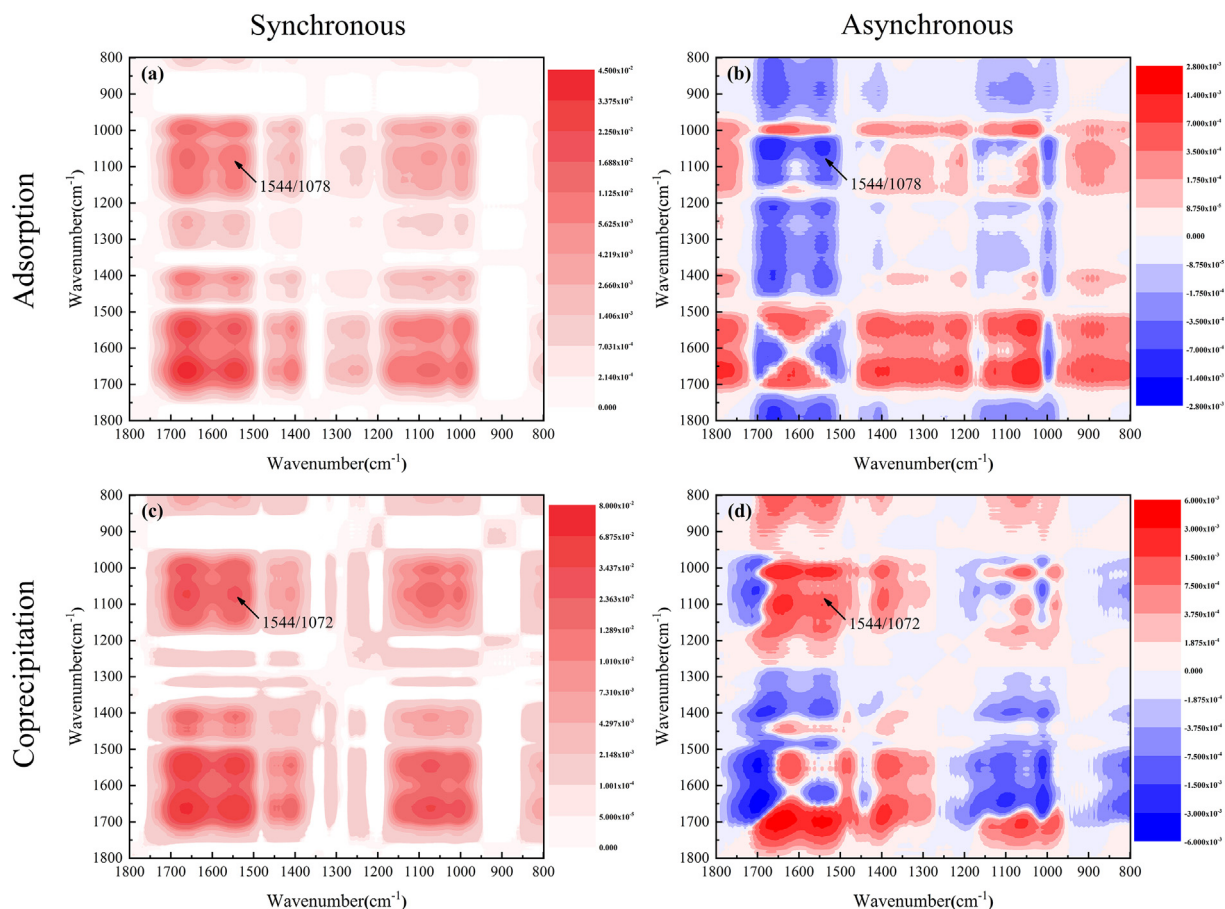
Fig. 7. Synchronous and asynchronous 2D spectra in the 1800–800 cm^{-1} region for the adsorption complexes (a, b) and coprecipitates (c, d) with EPS concentration as the perturbation variable. The red (blue) regions are defined as positive (negative) correlation intensities. Exemplary label (1544/1078 or 1544/1072) represents the cross peak between amide II (1544 cm^{-1}) and nucleic acid P=O/polysaccharide C—O—C (1078; 1072 cm^{-1}).

that EPS components interact with a continuum of Fe, Fe hydroxyl polymers and Fe (oxyhydr)oxides in coprecipitates, which favours the formation of an organomineral matrix (Pédrot et al., 2011; Mikutta et al., 2014). Furthermore, cross-linking of Fe(O, OH)$_6$ octahedral chains during coprecipitation might be disturbed to some extent by EPS compounds, resulting in slightly reduced crystalline structures (Eusterhues et al., 2008). Consequently, Fe (oxyhydr)oxides coprecipitated with EPS often exhibit less crystalline structure and thus lower X-ray diffraction intensity than their EPS-free analogues (Fig. A.2). At low C/Fe ratios (<1), in addition to the complexation of hydrolyzed Fe species with EPS and the coprecipitation of insoluble metal–organic complexes during the coprecipitation reaction (Chen et al., 2014), we also observe a high degree of adsorption of EPS onto the surface of the neoformed ferrihydrite particles. This is confirmed by the XPS results, which show that the surface to bulk C/(Fe + C) ratios in the coprecipitates are similar to those in the adsorption complexes at low C/Fe ratios (Table 2). The substantial occlusion of EPS at high C/Fe ratio, compared to the occlusion and adsorption of EPS at low C/Fe ratio during coprecipitation is also observed for

DOM (Han et al., 2019). Our results imply that the dominant mechanism of C retention by coprecipitation is regulated by the C/Fe ratio.

An increase in EPS content in coprecipitates effects both the particle size and structural order of Fh (Mikutta et al., 2008; Poggenburg et al., 2016), and also Fh surface reactivity (Poggenburg et al., 2018a). Here, although coprecipitates sorb more EPS, which is rich in negatively charged functional groups, compared to the adsorption complexes, the zeta potential values of the coprecipitates are always higher than those of the adsorption complexes at acidic or neutral pH (Fig. 3). This might be understood if more acidic groups are neutralized during the coprecipitation of EPS and Fe(III). Previous work shows that during the coprecipitation and adsorption of humic acid with ferrihydrite, the ionization of phenolic functional groups is inhibited to a higher degree in the coprecipitates than the adsorption complexes (Angelico et al., 2014). The pathway of formation (adsorption versus coprecipitation) of EPS-Fh couplings thus substantially affects the interfacial properties of the mineral phase, and thus the reactivity EPS organominerals in the environment (Han et al., 2019; Kikuchi et al., 2019).

4.2. Preferential adsorption and coprecipitation of EPS components with ferrihydrite

Chemical fractionation of EPS occurs during its interaction with minerals, as a result of the range in EPS molecular masses and functional group compositions (Omoike and Chorover, 2006). In this study, EPS-C and -N are both adsorbed to and coprecipitated with Fe (oxyhydr)oxide in a disproportionate manner, compared to the C/N ratio of unreacted EPS. This contrasts with previous work with Al (oxyhydr)oxides in which EPS-C and -N are proportionally adsorbed to and coprecipitated with Al phases (Mikutta et al., 2011), and suggests that EPS interactions with metal (oxyhydr)oxides are mineral specific. As a likely result of the higher loadings of EPS with Fe (oxyhydr)oxide coprecipitates compared to the lower loadings of EPS adsorption complexes (Fig. 1a; Table 1), the coprecipitates have higher total EPS-C and -N. However, the adsorption complexes are more selective towards the EPS components, resulting in greater mass fractionation of EPS-C and -N (Fig. 1b; Table 1). For EPS-P this study shows that EPS-P contained in monoesters and diesters of phospholipids, teichoic acids or nucleic acids is preferentially adsorbed and coprecipitated. This result is consistent with the results of previous studies of EPS interaction with goethite (Omoike and Chorover, 2006) and phospholipid interaction with hematite and goethite (Cagnasso et al., 2010). However, within the range of the molar C/Fe ratios investigated here, coprecipitation results in near-complete EPS-P sorption and thus little EPS-P fractionation, compared to during adsorption with Fe (oxyhydr)oxide (Fig. 2). These results suggest that the chemical specificity and steric accessibility of EPS components towards Fe species play an important role in EPS fractionation.

XPS and NEXAFS spectroscopy provide powerful and complementary molecular information about EPS fractionation during adsorption and coprecipitation with Fh. The work here shows that adsorption and coprecipitation of EPS with Fh generally shows differential effects with respect to EPS protein, polysaccharide and lipid species. In agreement with the bulk FTIR results for EPS characterization (Fig. A.4; Table 4), the C 1s XPS results suggest that upon EPS adsorption and coprecipitation, the relative contribution of aliphatic C representing EPS proteins and phospholipids is higher, compared to the unreacted EPS. This result is consistent with the preferential sorption of proteins and phospholipids during phospholipid interaction (as EPS P-containing moieties) with hematite and goethite (Cagnasso et al., 2010) and EPS interaction with Al (oxyhydr)oxide (Mikutta et al., 2011), and also with the fact that iron oxides selectively stabilize aliphatic compounds in simulated and natural soil systems (Adhikari and Yang, 2015; Wan et al., 2019). As the C/Fe ratio increases from 1, only during EPS adsorption does the percentage of amide C increase, and amide C decreases during coprecipitation, compared to the unreacted EPS (Fig. 5). Therefore, nucleic acids and proteins might be adsorbed onto Fh surfaces via both inner-sphere complexation and electrostatic mechanisms, as observed for EPS adsorption on goethite (Omoike and Chorover, 2006). In addition, it may be that

preferential incorporation of protein into the EPS coprecipitates results in a decrease in the percentage of surface amide C. The NEXAFS results further indicate that protein and acidic polysaccharide components are preferentially retained in the adsorption complexes, while more phospholipid and polysaccharide components are retained in the coprecipitates. These data indicate that the composition of Fh-EPS associations might be heterogeneous with distance from the mineral surface and zoned in larger and more complex Fh aggregates.

The reactivity and resulting selective retention of EPS with Fh may be substantially affected by the presence of competing inorganic anions (i.e., phosphate, silicate and bicarbonate) present in the natural environment. For adsorption systems, the presence of competitive oxyanions such as phosphate can markedly decrease the amount of OM adsorbed, depending on their ability to form stronger bonds on the surface of hydroxylated minerals than organic adsorbates (Chen et al., 2014; Kleber et al., 2015). The affect of competing oxyanions on EPS adsorption and whether adsorptive competition changes the amount and identity of the EPS components that are retained during adsorption and coprecipitation with iron (oxyhydr)oxides, compared to oxyanion free systems, is a subject for future work. For coprecipitation systems, Fe molecular speciation is an additional aspect that may be affected by competitive oxyanions. In particular the presence of silicate leads to the formation of Si-hydrous ferric oxide (HFO) under all conditions (van Genuchten et al., 2014). During coprecipitation these inorganic solutes can modify the structure, composition and identity of the Fe(III) coprecipitates, and thus potentially affect the selective retention of OM components at the mineral interface. Future work on the affect of competing oxyanions on EPS coprecipitation, compared to oxyanion free systems, should therefore investigate both mineral reactivity and EPS sorption and selective retention to form a more complete understanding of competing inorganic ion effects in natural environments.

4.3. Processes of preferential adsorption and coprecipitation of EPS components with ferrihydrite

In order to elucidate more detailed information on the preferential sorption of different EPS components during adsorption and coprecipitation with Fh, bulk FTIR and subsequently two dimensional (2D) FTIR correlation spectroscopy (COS) are employed. The FTIR results indicate that amide II is preferentially precipitated into coprecipitates relative to amide I in protein structures, but this phenomenon is not observed in adsorption complexes (Table 4). Analysis of the peak area ratios for the FTIR spectra reveal that more nucleic acid components are selectively retained in adsorption complexes, relative to protein components. These results indicate that adsorbed and coprecipitated EPS retain different protein subcomponents. Although the conventional one-dimensional FTIR approach can provide information on the compositional changes of the bulk EPS associated with Fh, even on semi-quantitative relative changes, one dimensional FTIR is unable to distinguish overlapping vibrational peaks and

thus provide more detailed molecular-level information. To solve this problem, 2D-FTIR-COS is used to enhance the spectral resolution and identify overlapping peaks (Noda, 2017).

2D-COS is a valuable mathematical tool for identifying the subtle responses of a heterogeneous mixture (e.g., EPS) under external perturbation (e.g. EPS concentration) (Lee and Hur, 2016). 2D-COS can also provide information on the extent and the sequence of the changes in the spectral intensity in different spectral regions. In summary of this study, 2D-FTIR-COS reveals that EPS amides are adsorbed and coprecipitated to a greater degree than other EPS components, and that EPS molecules relating to polysaccharide C-O-C are sorbed to a greater degree in coprecipitated rather than adsorbed EPS-Fh associations. Furthermore, 2D-FTIR-COS also reveals that the chemical complexation of carboxylate functional groups, occurring in polysaccharides, occurs prior to that of amide functional groups in the two EPS-Fh formation pathways. The chemical complexation of P=O functional groups, occurring in phospholipids, also occurs faster than the carboxylate and amide functional groups in the adsorption complexes, but slower than the carboxylate and amide functional groups in the coprecipitates. These results show that the mechanisms by which different EPS components are preferentially fixed by ferrihydrite via adsorption and coprecipitation are different.

For the adsorption complexes, work here is consistent with the "layer-by-layer onion" conceptual model of OC stabilization by minerals (Sollins et al., 2006), which we suggest might therefore provide a conceptual framework for understanding EPS adsorption on Fh. According to this model, carboxylated organics and multifunctional proteinaceous compounds form an adsorbed layer of OM on mineral surfaces, which provides a preconditioned surface onto which less polar hydrophilic and hydrophobic organics can sorb more readily than they would do onto clean mineral surfaces (Sollins et al., 2006). Our results are consistent with the adsorption of carboxylated and proteinaceous compounds in the EPS adsorption complexes because our XPS shows preferential enrichment of acidic polysacharrides and protein-like components, while our NEXAFS shows that carboxylic/amide C-containing components are selectively retained. Furthermore, our 2D-COS reveals that whilst the P=O functional groups are adsorbed faster than the amide and carboxylate functional groups, the complexation of carboxylate functional groups in acidic polysaccharides occurs prior to that of amide functional groups, suggesting that these are among the first groups to attach to the mineral surfaces.

The C 1s NEXAFS spectra of the adsorption complexes and coprecipitates are similar to those of natural Fh samples derived from acid mine drainage environments, in that they show a shoulder peak at 287.7 eV assigned to aliphatic C, which is consistent with a "layer-by-layer onion" model (Chan et al., 2009; Cismasu et al., 2011). Potential OC-OC interactions are also suggested to occur during the further adsorption and fractionation of OM derived from leaf litter on the surface of biogenic ferrihydrite, as revealed by Fourier transform ion cyclotron resonance mass spectrometry (FT-ICR-MS) (Sowers et al., 2019).

For the coprecipitates, work here suggests that EPS coprecipitation with Fh can be understood by considering that EPS components interact with a continuum of Fe, Fe hydroxyl polymers and Fe (oxyhydr)oxide (Fh) species, resulting in the embedding of acidic polysaccharides within the coprecipitates, and the binding of proteins, phospholipids and aliphatics around these organomineral clusters at their surfaces. Our results and previous STXM-NEXAFS studies (Chan et al., 2009; Cismasu et al., 2011) are consistent with the embedding of acidic polysaccharides in the coprecipitates, as visualised by CLSM (Fig. 4). Furthermore, as for the adsorption complexes, our 2D-COS results also show that the complexation of carboxylate functional groups in acidic polysaccharides occurs prior to that of amide functional groups. During a coprecipitation process this therefore suggests that carboxylate compounds interact with Fe and Fe hydroxyl polymers in the early stages of coprecipitation such that they become occluded into the resulting organomineral structures. Finally, unlike for the adsorption complexes, our 2D-COS results show that the P=O functional groups are adsorbed slower than the amide and carboxylate functional groups, suggesting that phospholipids might bind to the outer regions of the coprecipitates once the Fe hydroxyl polymers have formed Fh nanoparticles.

5. CONCLUSION

Experiments here reveal the mass fractionation behaviour of EPS during adsorption to and coprecipitation with ferrihydrite. We find that EPS is fractionated during both adsorption and coprecipitation reactions. Compared to unreacted EPS, our results indicate that aliphatic C is preferentially adsorbed and coprecipitated compared with carbohydrate C, but that amide C increases during adsorption and decreases during coprecipitation. We also find that proteins and acidic polysaccharides are preferentially retained in the adsorption complexes, and lipids and polysaccharide components are retained in the coprecipitates. At initial C/Fe ratio ≥ 1, EPS-ferrihydrite coprecipitates are loaded with a high content of EPS-C, and EPS-ferrihydrite adsorption complexes preferentially retain EPS-N. Due to the higher overall mass fraction of EPS-C in EPS-ferrihydrite coprecipitates however, EPS-ferrihydrite coprecipitates show a less substantial EPS mass fractionation. 2D-FTIR-COS further reveals that in the two EPS-ferrihydrite formation pathways, the chemical complexation of carboxylate functional groups during the reaction of EPS and Fe occurs prior to that of amide functional groups. The P=O functional groups, however, are adsorbed onto ferrihydrite faster than the carboxylate and amide functional groups, and the P=O functional groups are coprecipitated with Fe species slower than the carboxylate and amide functional groups. Although the EPS-Fh coprecipitates retain a higher amount of EPS, the XRD patterns of the adsorption complexes show a more obvious additional peak from the EPS, and the zeta potential values of the adsorption complexes are always lower than those of

the coprecipitates. Our results thus indicate that more acidic groups are embedded and neutralized during EPS coprecipitation with Fe species. Although different EPS can have different biochemical compositions, all EPS contains an abundance of the reactive functional groups known to interact with Fe (oxyhydr)oxides (Omoike and Chorover, 2006). Our results are therefore expected to be widely applicable to EPS from different bacterial sources. Overall our findings indicate that the formation pathway of EPS-ferrihydrite associations plays an important role in the binding and selective retention of EPS components and thus in controlling the reactivity and cycling of microbially-derived OC, like EPS, in soils. This study provides new insight into the coupling between the fate of microbially-derived compounds and Fe cycling in natural environments.

Declaration of Competing Interest

The authors declare that they have no known competing financial interests or personal relationships that could have appeared to influence the work reported in this paper.

ACKNOWLEDGEMENTS

RESEARCH DATA

Research Data associated with this article can be accessed at Mendeley Data Repository: https://doi.org/10.17632/49hbdyz6zk.2.

APPENDIX A. SUPPLEMENTARY MATERIAL

Supplementary data to this article can be found online at https://doi.org/10.1016/j.gca.2021.02.015.

REFERENCES

Adhikari D. and Yang Y. (2015) Selective stabilization of aliphatic organic carbon by iron oxide. *Sci. Rep.* **5**, 11214.

Angelico R., Ceglie A., He J.-Z., Liu Y.-R., Palumbo G. and Colombo C. (2014) Particle size, charge and colloidal stability of humic acids coprecipitated with Ferrihydrite. *Chemosphere* **99**, 239–247.

Basile-Doelsch I., Balesdent J. and Pellerin S. (2020) Reviews and syntheses: The mechanisms underlying carbon storage in soil. *Biogeosci. Discuss.*, 1–33.

Beveridge T. J., Makin S. A., Kadurugamuwa J. L. and Li Z. (1997) Interactions between biofilms and the environment. *FEMS Microbiol. Rev.* **20**, 291–303.

Cagnasso M., Boero V., Franchini M. A. and Chorover J. (2010) ATR-FTIR studies of phospholipid vesicle interactions with α-FeOOH and α-Fe2O3 surfaces. *Colloids Surf. B Biointerfaces* **76**, 456–467.

Cai P., Lin D., Peacock C. L., Peng W. and Huang Q. (2018) EPS adsorption to goethite: Molecular level adsorption mechanisms using 2D correlation spectroscopy. *Chem. Geol.* **494**, 127–135.

Cao Y., Wei X., Cai P., Huang Q., Rong X. and Liang W. (2011) Preferential adsorption of extracellular polymeric substances from bacteria on clay minerals and iron oxide. *Colloids Surf. B Biointerfaces* **83**, 122–127.

Chan C. S., Fakra S. C., Edwards D. C., Emerson D. and Banfield J. F. (2009) Iron oxyhydroxide mineralization on microbial extracellular polysaccharides. *Geochim. Cosmochim. Acta* **73**, 3807–3818.

Chen C., Dynes J. J., Wang J. and Sparks D. L. (2014) Properties of Fe-organic matter associations via coprecipitation versus adsorption. *Environ. Sci. Technol.* **48**, 13751–13759.

Chenu C. (1993) Clay- or sand-polysaccharide associations as models for the interface between micro-organisms and soil: water related properties and microstructure. *Geoderma* **56**, 143–156.

Chenu C. and Cosentino D. (2011) Microbial regulation of soil structural dynamics. In *The Architecture and Biology of Soils: Life in Inner Space* (eds. K. Ritz and I. Young). CABI, Wallingford, pp. 37–70.

Chin Y.-P., Traina S. J., Swank C. R. and Backhus D. (1998) Abundance and properties of dissolved organic matter in pore waters of a freshwater wetland. *Limnol. Oceanogr.* **43**, 1287–1296.

Cismasu A. C., Michel F. M., Tcaciuc A. P., Tyliszczak T. and Brown, Jr, G. E. (2011) Composition and structural aspects of naturally occurring ferrihydrite. *Comptes Rendus Geosci.* **343**, 210–218.

Cornell R. M. and Schwertmann U. (2003) *The Iron Oxides: Structure, Properties, Reactions, Occurrences, and Uses*, 2nd, completely rev. and extended ed ed. Wiley-VCH, Weinheim.

Costa O. Y. A., Raaijmakers J. M. and Kuramae E. E. (2018) Microbial extracellular polymeric substances: ecological function and impact on soil aggregation. *Front. Microbiol.* **9**, 1636.

Couasnon T., Gélabert A., Ona-Nguema G., Zanna S., Ménez B. and Guyot F. (2019) Experimental assessment of occurrences and stability of lead-bearing minerals in bacterial biofilms. *Chem. Geol.* **505**, 23–35.

Domínguez-Vidal A., Saenz-Navajas M. P., Ayora-Cañada M. J. and Lendl B. (2006) Detection of albumin unfolding preceding proteolysis using fourier transform infrared spectroscopy and chemometric data analysis. *Anal. Chem.* **78**, 3257–3264.

Dublet G., Lezama P. J., Bargar J. R., Fendorf S., Kumar N., Lowry G. V. and Brown G. E. (2017) Partitioning of uranyl between ferrihydrite and humic substances at acidic and circum-neutral pH. *Geochim. Cosmochim. Acta* **215**, 122–140.

DuBois Miche, Gilles K. A., Hamilton J. K., Rebers P. A. and Fred S. (1956) Colorimetric method for determination of sugars and related substances. *Anal. Chem.* **28**, 350–356.

Eusterhues K., Rennert T., Knicker H., Kögel-Knabner I., Totsche K. U. and Schwertmann U. (2011) Fractionation of organic

matter due to reaction with ferrihydrite: coprecipitation versus adsorption. *Environ. Sci. Technol.* **45**, 527–533.

Eusterhues K., Wagner F. E., Häusler W., Hanzlik M., Knicker H., Totsche K. U., Kögel-Knabner I. and Schwertmann U. (2008) Characterization of ferrihydrite-soil organic matter coprecipitates by X-ray diffraction and Mössbauer spectroscopy. *Environ. Sci. Technol.* **42**, 7891–7897.

Fang L., Cao Y., Huang Q., Walker S. L. and Cai P. (2012) Reactions between bacterial exopolymers and goethite: a combined macroscopic and spectroscopic investigation. *Water Res.* **46**, 5613–5620.

Ferris F. G. (2005) Biogeochemical properties of bacteriogenic iron oxides. *Geomicrobiol. J.* **22**, 79–85.

Flemming H.-C. and Wingender J. (2010) The biofilm matrix. *Nat. Rev. Microbiol.* **8**, 623–633.

Flemming H.-C., Neu T. R. and Wingender J. (2016) *The Perfect Slime: Microbial Extracellular Polymeric Substances (EPS)*. IWA Publishing.

Fortin D. and Langley S. (2005) Formation and occurrence of biogenic iron-rich minerals. *Earth-Sci. Rev.* **72**, 1–19.

Fritzsche A., Schröder C., Wieczorek A. K., Händel M., Ritschel T. and Totsche K. U. (2015) Structure and composition of Fe–OM co-precipitates that form in soil-derived solutions. *Geochim. Cosmochim. Acta* **169**, 167–183.

Gu B., Schmitt J., Chen Z., Liang L. and McCarthy J. F. (1994) Adsorption and desorption of natural organic matter on iron oxide: mechanisms and models. *Environ. Sci. Technol.* **28**, 38–46.

Gu B., Schmitt J., Chen Z., Liang L. and McCarthy J. F. (1995) Adsorption and desorption of different organic matter fractions on iron oxide. *Geochim. Cosmochim. Acta* **59**, 219–229.

Guibaud G., Bordas F., Saaid A., D'abzac P. and Van Hullebusch E. (2008) Effect of pH on cadmium and lead binding by extracellular polymeric substances (EPS) extracted from environmental bacterial strains. *Colloids Surf. B Biointerfaces* **63**, 48–54.

Han L., Sun K., Keiluweit M., Yang Y. u., Yan Y., Jin J., Sun H., Wu F. and Xing B. (2019) Mobilization of ferrihydrite-associated organic carbon during Fe reduction: adsorption versus coprecipitation. *Chem. Geol.* **503**, 61–68.

Henneberry Y. K., Kraus T. E. C., Nico P. S. and Horwath W. R. (2012) Structural stability of coprecipitated natural organic matter and ferric iron under reducing conditions. *Organic Geochem.* **48**, 81–89.

Hofmann A., Pelletier M., Michot L., Stradner A., Schurtenberger P. and Kretzschmar R. (2004) Characterization of the pores in hydrous ferric oxide aggregates formed by freezing and thawing. *J. Colloid Interface Sci.* **271**, 163–173.

Huang W., Ertekin E., Wang T., Cruz L., Dailey M., DiRuggiero J. and Kisailus D. (2020) Mechanism of water extraction from gypsum rock by desert colonizing microorganisms. *PNAS* **117**, 10681–10687.

Jia Q., Wang N.-N. and Yu Z.-W. (2009) An insight into sequential order in two-dimensional correlation spectroscopy. *Appl. Spectrosc.* **63**, 344–353.

Jubb A. M., Eskelsen J. R., Yin X., Zheng J., Philben M. J., Pierce E. M., Graham D. E., Wullschleger S. D. and Gu B. (2018) Characterization of iron oxide nanoparticle films at the air–water interface in Arctic tundra waters. *Sci. Total Environ.* **633**, 1460–1468.

Kaiser K. and Guggenberger G. (2007) Sorptive stabilization of organic matter by microporous goethite: sorption into small pores vs. surface complexation. *Eur. J. Soil Sci.* **58**, 45–59.

Kaiser K. and Guggenberger G. (2000) The role of DOM sorption to mineral surfaces in the preservation of organic matter in soils. *Org. Geochem.* **31**, 711–725.

Kallenbach C. M., Frey S. D. and Grandy A. S. (2016) Direct evidence for microbial-derived soil organic matter formation and its ecophysiological controls. *Nat. Commun.* **7**, 13630.

Katoh M., Murase J., Hayashi M., Matsuya K. and Kimura M. (2004) Nutrient leaching from the plow layer by water percolation and accumulation in the subsoil in an irrigated paddy field. *Soil Sci. Plant Nutr.* **50**, 721–729.

Kikuchi S., Kashiwabara T., Shibuya T. and Takahashi Y. (2019) Molecular-scale insights into differences in the adsorption of cesium and selenium on biogenic and abiogenic ferrihydrite. *Geochim. Cosmochim. Acta* **251**, 1–14.

Kinyangi J., Solomon D., Liang B., Lerotic M., Wirick S. and Lehmann J. (2006) Nanoscale biogeocomplexity of the organomineral assemblage in soil. *Soil Sci. Soc. Am. J.* **70**, 1708–1718.

Kleber M., Eusterhues K., Keiluweit M., Mikutta C., Mikutta R. and Nico P. S. (2015) Mineral–organic associations: formation, properties, and relevance in soil environments. In *Advances in Agronomy* (ed. D. L. Sparks). Academic Press, pp. 1–140.

Kovács Á. T. (2019) Bacillus subtilis. *Trends in Microbiology* **27**, 724–725.

Lalonde K., Mucci A., Ouellet A. and Gélinas Y. (2012) Preservation of organic matter in sediments promoted by iron. *Nature* **483**, 198–200.

Lawrence J. R., Swerhone G. D. W., Leppard G. G., Araki T., Zhang X., West M. M. and Hitchcock A. P. (2003) Scanning transmission X-Ray, laser scanning, and transmission electron microscopy mapping of the exopolymeric matrix of microbial biofilms. *Appl. Environ. Microbiol.* **69**, 5543–5554.

Lee B.-M. and Hur J. (2016) Adsorption behavior of extracellular polymeric substances on graphene materials explored by fluorescence spectroscopy and two-dimensional fourier transform infrared correlation spectroscopy. *Environ. Sci. Technol.* **50**, 7364–7372.

Li H., Hu S., Polizzotto M. L., Chang X., Shen Q., Ran W. and Yu G. (2016) Fungal biomineralization of montmorillonite and goethite to short-range-ordered minerals. *Geochim. Cosmochim. Acta* **191**, 17–31.

Liang C. and Balser T. C. (2011) Microbial production of recalcitrant organic matter in global soils: implications for productivity and climate policy. *Nat. Rev. Microbiol.* **9**, 75.

Lin D., Cai P., Peacock C. L., Wu Y., Gao C., Peng W., Huang Q. and Liang W. (2018) Towards a better understanding of the aggregation mechanisms of iron (hydr)oxide nanoparticles interacting with extracellular polymeric substances: role of pH and electrolyte solution. *Sci. Total Environ.* **645**, 372–379.

Lin D., Ma W., Jin Z., Wang Y., Huang Q. and Cai P. (2016) Interactions of EPS with soil minerals: a combination study by ITC and CLSM. *Colloids Surf. B Biointerfaces* **138**, 10–16.

Liu X., Eusterhues K., Thieme J., Ciobota V., Höschen C., Mueller C. W., Küsel K., Kögel-Knabner I., Rösch P., Popp J. and Totsche K. U. (2013) STXM and NanoSIMS investigations on EPS fractions before and after adsorption to goethite. *Environ. Sci. Technol.* **47**, 3158–3166.

Lv J., Zhang S., Wang S., Luo L., Cao D. and Christie P. (2016) Molecular-scale investigation with ESI-FT-ICR-MS on fractionation of dissolved organic matter induced by adsorption on iron oxyhydroxides. *Environ. Sci. Technol.* **50**, 2328–2336.

Ma W., Peng D., Walker S. L., Cao B., Gao C.-H., Huang Q. and Cai P. (2017) Bacillus subtilis biofilm development in the presence of soil clay minerals and iron oxides. *Npj Biofilms Microbiomes* **3**, 1–9.

Mikutta C., Mikutta R., Bonneville S., Wagner F., Voegelin A., Christl I. and Kretzschmar R. (2008) Synthetic coprecipitates of exopolysaccharides and ferrihydrite. Part I: Characterization. *Geochim. Cosmochim. Acta* **72**, 1111–1127.

Mikutta R., Baumgärtner A., Schippers A., Haumaier L. and Guggenberger G. (2012) Extracellular polymeric substances from bacillus subtilis associated with minerals modify the extent and rate of heavy metal sorption. *Environ. Sci. Technol.* **46**, 3866–3873.

Mikutta R., Lorenz D., Guggenberger G., Haumaier L. and Freund A. (2014) Properties and reactivity of Fe-organic matter associations formed by coprecipitation versus adsorption: clues from arsenate batch adsorption. *Geochim. Cosmochim. Acta* **144**, 258–276.

Mikutta R., Mikutta C., Kalbitz K., Scheel T., Kaiser K. and Jahn R. (2007) Biodegradation of forest floor organic matter bound to minerals via different binding mechanisms. *Geochim. Cosmochim. Acta* **71**, 2569–2590.

Mikutta R., Zang U., Chorover J., Haumaier L. and Kalbitz K. (2011) Stabilization of extracellular polymeric substances (Bacillus subtilis) by adsorption to and coprecipitation with Al forms. *Geochim. Cosmochim. Acta* **75**, 3135–3154.

Miltner A., Bombach P., Schmidt-Brücken B. and Kästner M. (2012) SOM genesis: microbial biomass as a significant source. *Biogeochemistry* **111**, 41–55.

Noda I. (2017) Vibrational two-dimensional correlation spectroscopy (2DCOS) study of proteins. *Spectrochim. Acta. A. Mol. Biomol. Spectrosc.* **187**, 119–129.

Noda I. and Ozaki Y. (2004) *Two-Dimensional Correlation Spectroscopy - Applications in Vibrational and Optical Spectroscopy*. John Wiley & Sons Ltd, Chichester, UK.

Omoike A. and Chorover J. (2006) Adsorption to goethite of extracellular polymeric substances from Bacillus subtilis. *Geochim. Cosmochim. Acta* **70**, 827–838.

Omoike A. and Chorover J. (2004) Spectroscopic study of extracellular polymeric substances from bacillus subtilis: aqueous chemistry and adsorption effects. *Biomacromolecules* **5**, 1219–1230.

Or D., Phutane S. and Dechesne A. (2007) Extracellular polymeric substances affecting pore-scale hydrologic conditions for bacterial activity in unsaturated soils. *Vadose Zone J.* **6**, 298–305.

Pédrot M., Boudec A. L., Davranche M., Dia A. and Henin O. (2011) How does organic matter constrain the nature, size and availability of Fe nanoparticles for biological reduction? *J. Colloid Interface Sci.* **359**, 75–85.

Poggenburg C., Mikutta R., Liebmann P., Koch M. and Guggenberger G. (2018a) Siderophore-promoted dissolution of ferrihydrite associated with adsorbed and coprecipitated natural organic matter. *Org. Geochem.* **125**, 177–188.

Poggenburg C., Mikutta R., Sander M., Schippers A., Marchanka A., Dohrmann R. and Guggenberger G. (2016) Microbial reduction of ferrihydrite-organic matter coprecipitates by Shewanella putrefaciens and Geobacter metallireducens in comparison to mediated electrochemical reduction. *Chem. Geol.* **447**, 133–147.

Poggenburg C., Mikutta R., Schippers A., Dohrmann R. and Guggenberger G. (2018b) Impact of natural organic matter coatings on the microbial reduction of iron oxides. *Geochim. Cosmochim. Acta* **224**, 223–248.

Ravel B. and Newville M. (2005) ATHENA, ARTEMIS, HEPHAESTUS: data analysis for X-ray absorption spectroscopy using IFEFFIT. *J Synchrotron Rad* **12**, 537–541.

Schmidt M. P. and Martínez C. E. (2016) Kinetic and conformational insights of protein adsorption onto montmorillonite revealed using in situ ATR-FTIR/2D-COS. *Langmuir* **32**, 7719–7729.

Simpson A. J., Simpson M. J., Smith E. and Kelleher B. P. (2007) Microbially derived inputs to soil organic matter: are current estimates too low? *Environ. Sci. Technol.* **41**, 8070–8076.

Sollins P., Swanston C., Kleber M., Filley T., Kramer M., Crow S., Caldwell B. A., Lajtha K. and Bowden R. (2006) Organic C and N stabilization in a forest soil: evidence from sequential density fractionation. *Soil Biol. Biochem.* **38**, 3313–3324.

Solomon D., Lehmann J., Kinyangi J., Liang B., Heymann K., Dathe L., Hanley K., Wirick S. and Jacobsen C. (2009) Carbon (1s) NEXAFS spectroscopy of biogeochemically relevant reference organic compounds. *Soil Sci. Soc. Am. J.* **73**, 1817–1830.

Sowers T. D., Adhikari D., Wang J., Yang Y. and Sparks D. L. (2018) Spatial associations and chemical composition of organic carbon sequestered in Fe, Ca, and organic carbon ternary systems. *Environ. Sci. Technol.* **52**, 6936–6944.

Sowers T. D., Holden K. L., Coward E. K. and Sparks D. L. (2019) Dissolved organic matter sorption and molecular fractionation by naturally occurring bacteriogenic iron (oxyhydr)oxides. *Environ. Sci. Technol.* **53**, 4295–4304.

Sze A., Erickson D., Ren L. and Li D. (2003) Zeta-potential measurement using the Smoluchowski equation and the slope of the current–time relationship in electroosmotic flow. *J. Colloid Interface Sci.* **261**, 402–410.

van Genuchten C. M., Peña J., Amrose S. E. and Gadgil A. J. (2014) Structure of Fe(III) precipitates generated by the electrolytic dissolution of Fe(0) in the presence of groundwater ions. *Geochim. Cosmochim. Acta* **127**, 285–304.

Wagai R. and Mayer L. M. (2007) Sorptive stabilization of organic matter in soils by hydrous iron oxides. *Geochim. Cosmochim. Acta* **71**, 25–35.

Wan D., Ye T., Lu Y., Chen W., Cai P. and Huang Q. (2019) Iron oxides selectively stabilize plant-derived polysaccharides and aliphatic compounds in agricultural soils. *Eur. J. Soil Sci.* **70**, 1153–1163.

Wu Y., Cai P., Jing X., Niu X., Ji D., Ashry N. M., Gao C. and Huang Q. (2019) Soil biofilm formation enhances microbial community diversity and metabolic activity. *Environ. Int.* **132** 105116.

Xu X., Thornton P. E. and Post W. M. (2013) A global analysis of soil microbial biomass carbon, nitrogen and phosphorus in terrestrial ecosystems. *Glob. Ecol. Biogeogr.* **22**, 737–749.

Yan S., Cai Y., Li H., Song S. and Xia L. (2019) Enhancement of cadmium adsorption by EPS-montmorillonite composites. *Environ. Pollut.* **252**, 1509–1518.

Yan W., Wang H. and Jing C. (2016) Adhesion of shewanella oneidensis MR-1 to goethite: a two-dimensional correlation spectroscopic study. *Environ. Sci. Technol.* **50**, 4343–4349.

Zhang R., Neu T. R., Zhang Y., Bellenberg S., Kuhlicke U., Li Q., Sand W. and Vera M. (2015) Visualization and analysis of EPS glycoconjugates of the thermoacidophilic archaeon Sulfolobus metallicus. *Appl. Microbiol. Biotechnol.* **99**, 7343–7356.

Associate Editor: Owen Duckworth